Monthly Notices
of the
ROYAL ASTRONOMICAL SOCIETY

MNRAS **428,** 2901–2920 (2013) doi:10.1093/mnras/sts227

Suzaku observations of 'bare' active galactic nuclei

D. J. Walton,[1,2]⋆ E. Nardini,[3] A. C. Fabian,[1] L. C. Gallo[4] and R. C. Reis[5]

[1]*Institute of Astronomy, Cambridge University, Madingley Road, Cambridge CB3 0HA*
[2]*Space Radiation Laboratory, California Institute of Technology, Pasadena, CA 91125, USA*
[3]*Harvard–Smithsonian Center for Astrophysics, 60 Garden Street, Cambridge, MA 02138, USA*
[4]*Department of Astronomy and Physics, Saint Mary's University, 923 Robie Street, Halifax, NS B3H 3C3, Canada*
[5]*Department of Astronomy, University of Michigan, 500 Church Street, Ann Arbor, MI 48109, USA*

Accepted 2012 October 16. Received 2012 October 13; in original form 2012 July 9

ABSTRACT

We present an X-ray spectral analysis of a large sample of 25 'bare' active galactic nuclei (AGN), sources with little or no complicating intrinsic absorption, observed with *Suzaku*. Our work focuses on studying the potential contribution from relativistic disc reflection and examining the implications of this interpretation for the intrinsic spectral complexities frequently displayed by AGN in the X-ray bandpass. During the analysis, we take the unique approach of attempting to simultaneously undertake a systematic analysis of the whole sample, as well as a detailed treatment of each individual source, and find that disc reflection has the required flexibility to successfully reproduce the broad-band spectrum observed for all of the sources considered. Where possible, we use the reflected emission to place constraints on the black hole spin for this sample of sources. Our analysis suggests a general preference for rapidly rotating black holes, which if taken at face value is most consistent with the scenario in which supermassive black hole growth is dominated by prolonged, ordered accretion. However, there may be observational biases towards AGN with high spin in the compiled sample, limiting our ability to draw strong conclusions for the general population at this stage. Finally, contrary to popular belief, our analysis also implies that the dichotomy between radio-loud/radio-quiet AGN is not solely related to black hole spin.

Key words: black hole physics – galaxies: active.

1 INTRODUCTION

Knowledge of the spin distribution for the supermassive black holes (SMBHs) powering active galactic nuclei (AGN) provides important information on the growth history of these black holes, which would otherwise be difficult to observationally constrain. The accretion and merger events experienced by these nuclear black holes over their lifetimes can impart enough angular momentum to substantially modify the black hole spins from their natal values (Moderski & Sikora 1996; Volonteri et al. 2005). Recent simulations by Berti & Volonteri (2008) demonstrate that the exact spin distribution expected depends strongly on the nature of these events, and in particular how the angular momentum of the accreted material/coalesced black holes relate to one another. If the accretion is primarily 'ordered', i.e. the accreted material has angular momentum in the same sense as that of the black hole, the black holes are spun up and will preferentially display high spins. If instead the accretion is chaotic, i.e. the angular momenta of the accreted material and the AGN are not typically aligned, the opposite will be true, leading to a strong preference for non-rotating black holes.

Measuring black hole spin requires knowledge of the radius of the innermost stable circular orbit (ISCO). Under the assumption that the inner accretion disc extends in to this radius, the ISCO can be measured through study of the reflected emission produced as the optically thick disc is irradiated by the hard X-rays generated in the corona, most likely via Compton upscattering. This emission contains a combination of backscattered continuum emission and atomic features lines, the most prominent of which is often the iron Kα emission line (6.4–6.97 keV, depending on ionization state) owing to its high cosmic abundance and fluorescent yield (see e.g. George & Fabian 1991). The reflected emission from the inner disc is blurred and broadened by the strong Doppler and relativistic effects inherent to material in close orbit around a black hole (Fabian et al. 1989; Laor 1991). This can result in broad and skewed observed emission lines profiles, even though the atomic emission is intrinsically narrow, and if the amount of relativistic blurring can be constrained, the inner radius of the disc can be quantified. Active galaxies do often display broad emission features that can be associated with relativistically broadened iron lines (see e.g. Tanaka et al. 1995; Nandra et al. 1999, 2007; Fabian et al. 2000, 2009), and

⋆ E-mail: dwalton@ast.cam.ac.uk

although questions have been raised over whether this is the correct interpretation for these features, with absorption-based models proposed as an alternative (Miller, Turner & Reeves 2008, 2009), in Walton et al. (2012) we present a strong argument in favour of the relativistic disc reflection origin through comparison with the similar features frequently observed in Galactic black hole binaries (BHBs).

Although the iron Kα line is frequently the most prominent reflected feature, for a broad range of ionization states the full reprocessed emission spectrum also contains a host of other emission lines from lighter elements at lower energies. In addition, reflection spectra also display a broad emission feature peaking at $\sim$30 keV, referred to as the Compton hump, due to the combined effects of photoelectric absorption of photons at lower energies and Compton downscattering of photons at higher energies. In order to self-consistently treat the reflected emission arising from the inner regions of the accretion disc, the same processes that broaden and skew the iron line must be applied to all of these features. These effects can blend the soft complex of reflected emission lines together into a smooth emission feature, offering a natural explanation for the soft excess frequently observed in the spectra of AGN (Crummy et al. 2006). Therefore, where possible, the broad-band spectra covering all the key reflected emission features should be considered when attempting to constrain the spin of AGN, and in principle it should be possible to constrain the spin from the broad-band spectrum even for sources that lack prominent broad iron lines, assuming the soft excess is indeed associated with reflection.

The best sources with which to perform such analysis and rigorously test the reflection interpretation are therefore 'bare' active galaxies, sources with little or no intrinsic absorption to complicate the determination of the reflected emission. Notable examples of such sources are Fairall 9 (Gondoin et al. 2001; Schmoll et al. 2009; Emmanoulopoulos et al. 2011a), Ark 120 (Vaughan et al. 2004; Nardini et al. 2011), Ton S180 (Vaughan et al. 2002; Nardini, Fabian & Walton 2012) and the extreme narrow-line Seyfert 1 galaxy 1H 0707−495 (Fabian et al. 2009).

However, even for apparently bare AGN, interpretations other than reflection have been proposed to explain the soft excess. Although bare AGN show little or no absorption by partially ionized material when studied by high-resolution grating spectrometers, it was suggested that the broad, overall curvature observed at low energies could still be caused by such absorption in an extremely turbulent outflow, in which large velocity broadening smears out the discrete atomic features (Gierliński & Done 2004; Middleton, Done & Gierliński 2007). However, more detailed simulations show that outflows driven from the disc are not actually able to provide the velocity broadening required (Schurch & Done 2007; Schurch, Done & Proga 2009). More recently, complex hybrid Comptonization interpretations have successfully been applied to the data, in which the soft excess arises due to Comptonization by thermal electrons within the inner disc, possibly existing as a skin-like layer on the surface of the disc, while the higher energy continuum arises in a separate, more traditional corona (Done et al. 2012; Jin, Ward & Done 2012).

Nevertheless, there is very good evidence to suggest that the soft excess does indeed arise due to reprocessing of the primary continuum. First of all, the energy of the soft excess is observed to be remarkably constant over many orders of magnitude in black hole mass and also over a fair range in Eddington ratio (Gierliński & Done 2004; Miniutti et al. 2009), which would require a roughly constant electron temperature in the Comptonization interpretation. Indeed, roughly constant electron temperatures were obtained by Done et al. (2012) and Jin et al. (2012). The temperature of the accretion disc is dependent on both black hole mass and Eddington ratio, and should vary substantially over the range of black hole masses and luminosities observed. It is probably not unreasonable to expect that some variation should also be seen in the temperature of the disc electrons over these ranges. The constant energy of this feature therefore strongly hints at an atomic origin which, given the inability of absorption to reproduce the soft excess highlighted previously, supports a reflection interpretation.

In addition, one of the key observational discoveries over the last couple of years is the detection of lags between the soft and hard X-ray emission, which demonstrate that, on short time-scales, the soft excess responds to changes in the high-energy continuum (Zoghbi et al. 2010; Zoghbi & Fabian 2011; Emmanoulopoulos, McHardy & Papadakis 2011b; de Marco et al. 2011), as predicted by the reflection-based interpretation. Although there have been claims that absorption-based interpretations can also reproduce these lags via reflection from the more distant obscuring clouds in the case of 1H 0707−495 (Miller et al. 2010), this requires both a special source geometry and viewing alignment, while evidence for such lags have now been seen in a large number of sources (De Marco et al. 2012), arguing strongly against this interpretation. Crucially, a similar lag has also now been detected between the high-energy continuum and the broad component of the iron line profile in NGC 4151 (Zoghbi et al. 2012), strongly suggesting that such lags are indeed characteristic for reflected emission. These lags also appear to argue strongly against the Comptonization interpretation, as fluctuations in the corona should not precede fluctuations in the inner disc.

In this paper, we present a reflection-based analysis of a sample of bare AGN, with the purpose of both testing the robustness of the reflection interpretation and, where possible, providing initial spin constraints for the AGN considered. We specifically focus on *Suzaku* observations in this work in order to utilize its combination of broad-band spectral coverage and large collecting area. The paper is structured as follows. Section 2 describes our data reduction and sample selection procedure, and Section 3 details our spectral analysis. We discuss our results in Section 4 and finally summarize our conclusions in Section 5.

2 OBSERVATIONS AND DATA REDUCTION

2.1 Data reduction

We reduced all the *Suzaku* observations of type 1 AGN publicly available prior to 2010 October. Using the latest HEASOFT software package, we processed the unfiltered event files for each of the XIS CCDs and editing modes operational in the respective observations, following the *Suzaku* Data Reduction Guide.[1] We started by creating new cleaned event files for all the XIS detectors operational during each observation (note that XIS2, one of the front-illuminated detectors, experienced a charge leak in 2006 November and has not been in operation since) by re-running the *Suzaku* pipeline with the latest calibration, as well as the associated screening criteria files. In addition to the standard XIS event selection criteria, we also required that the cut-off rigidity for clean events be greater than 6 GeV. The exact size of the circular source regions used varied from source to source, depending on, e.g., the presence of other nearby sources, but were typically $\sim$3.5 arcmin in radius, and background regions were selected from the surrounding areas on the CCD free of any

[1] http://heasarc.gsfc.nasa.gov/docs/suzaku/analysis/

Table 1. Observational details for the sample of 'bare' AGN compiled in this work, ordered in terms of the total XIS counts recorded. The uncertainties quoted on the XIS count rates are the 1σ uncertainties, while the PIN source rates are quoted as a percentage of the total rate recorded by the detector. Galactic column densities are taken from Kalberla et al. (2005), and positions and redshifts are compiled from the NASA Extragalactic Database (NED).

Source	RA (h:m:s)	Dec. (d:m:s)	z	$N_{\rm H,\,Gal}$ (10^{20} cm^{-2})	ObsID	Obs. date	Exposure (XIS/PIN; ks)	FI XIS rate (count s^{-1})	PIN per cent
Mrk 509	20:44:09.7	−10:43:25	0.0344	4.25	701093010	25/04/2006	22/15	3.446 ± 0.008	30
					701093020	14/10/2006	24/22	4.416 ± 0.008	25
					701093030	15/11/2006	18/17	4.42 ± 0.01	24
					701093040	27/11/2006	28/28	3.821 ± 0.008	23
3C 382	18:35:03.4	+32:41:47	0.05787	6.98	702125010	01/11/2007	120/114	3.075 ± 0.004	22
Mrk 335	00:06:19.5	+20:12:10	0.0258	3.56	701031010	21/06/2006	151/132	1.569 ± 0.002	7
Fairall 9	01:23:45.8	−58:48:20	0.0470	3.16	702043010	07/06/2007	145/127	1.963 ± 0.003	15
1H 0419−577	04:26:00.8	−57:12:00	0.1040	1.26	702041010	25/07/2007	179/161	1.453 ± 0.002	14
					704064010	16/01/2010	119/107	0.953 ± 0.002	7
Ark 564	22:42:39.3	+29:43:31	0.0247	5.34	702117010	26/06/2007	89/110	2.678 ± 0.004	7
Ark 120	05:16:11.4	−00:08:59	0.0327	9.78	702014010	01/04/2007	91/104	2.240 ± 0.004	16
3C 390.3	18:42:09.0	+79:46:17	0.0561	3.47	701060010	14/12/2006	91/92	2.083 ± 0.004	22
PKS 0558−504	05:59:47.4	−50:26:52	0.1372	3.36	701011010	17/01/2007	21/18	1.415 ± 0.006	8
					701011020	18/01/2007	19/17	2.001 ± 0.007	6
					701011030	19/01/2007	21/18	1.251 ± 0.006	4
					701011040	20/01/2007	20/16	2.049 ± 0.007	7
					701011050	21/01/2007	20/15	2.078 ± 0.007	5
NGC 7469	23:03:15.6	+08:52:26	0.0163	4.45	703028010	24/06/2008	92/85	1.258 ± 0.003	19
Mrk 110	09:25:12.9	+52:17:11	0.0353	1.30	702124010	02/11/2007	91/80	1.414 ± 0.003	13
Swift J0501.9−3239	05:19:35.8	−32:39:28	0.0124	1.75	703014010	11/04/2008	36/34	2.362 ± 0.006	22
Mrk 841	15:04:01.2	+10:26:16	0.0364	2.22	701084010	22/01/2007	45/41	0.950 ± 0.003	12
					701084020	23/07/2007	45/60	0.961 ± 0.003	12
Ton S180	00:57:19.9	−22:22:59	0.0620	1.36	701021010	09/12/2006	121/102	0.820 ± 0.002	4
PDS 456	17:28:19.8	−14:15:56	0.1840	19.6	701056010	24/02/2007	174/209	0.381 ± 0.001	2
1H 0323+342	03:24:41.1	+34:10:46	0.0610	12.7	704034010	26/07/2009	76/69	0.559 ± 0.002	11
UGC 6728	11:45:16.0	+79:40:53	0.0065	4.42	704029010	06/06/2009	46/39	0.897 ± 0.003	14
Mrk 359	01:27:32.5	+19:10:44	0.0174	4.26	701082010	06/02/2007	98/96	0.307 ± 0.001	4
MCG−2-14-9	05:16:21.2	−10:33:41	0.0285	7.13	703060010	28/08/2008	131/120	0.217 ± 0.001	5
ESO 548-G081	03:42:03.7	−21:14:40	0.0145	2.29	704026010	03/08/2009	39/33	0.661 ± 0.003	15
Mrk 1018	02:06:16.0	−00:17:29	0.0424	2.43	704044010	03/07/2009	37/35	0.548 ± 0.003	13
RBS 1124	12:31:36.4	+70:44:14	0.2080	1.52	702114010	14/04/2007	79/83	0.241 ± 0.001	10
IRAS 13224−3809	13:12:19.4	−38:24:53	0.0658	5.34	701003010	26/01/2007	166/159	0.102 ± 0.001	–
1H 0707−495	07:08:41.5	−49:33:06	0.0406	4.31	700008010	03/12/2005	121/137	0.060 ± 0.001	–
IRAS 05262+4432	05:29:55.5	+44:34:39	0.0322	32.1	703019010	12/09/2008	68/66	0.088 ± 0.001	–

contaminating sources, with care taken to avoid the calibration sources in the corners. XSELECT was used to extract spectral products from these event files, and responses were generated for each individual spectrum using the XISRESP script with a medium resolution. The spectra and response files for all the front-illuminated instruments, XIS0, XIS2 (where operational) and XIS3 were combined using the FTOOL ADDASCASPEC. Since we are interested in the average spectral properties of active galaxies in this work, where a source was observed on more than one occasion the individual spectra obtained from these observations were also combined into a single, averaged spectrum; for these sources, the spectra obtained from each of the individual observations were found to be broadly similar in each case. Finally, we grouped the spectra to have a minimum signal-to-noise ratio (S/N) of 5 per energy bin with the SPECGROUP task (part of the *XMM–Newton* SAS), to allow the use of χ^2 minimization during spectral fitting. During modelling, we do not consider the XIS spectra below 0.6 keV and also exclude the 1.7–2.5 keV energy range owing to calibration uncertainties, and we primarily make use of the front-illuminated spectra, owing to its superior performance at high energies, although the back-illuminated spectra are routinely checked for consistency.

For the HXD PIN detector, we again reprocessed the unfiltered event files for each of the observations considered following the data reduction guide. Since the HXD is a collimating instrument rather than an imaging spectrometer, estimating the background requires individual consideration of the non-X-ray instrumental background (NXB) and cosmic X-ray background (CXB). The response and NXB files were downloaded for each observation;[2] for all of the observations considered here the higher quality 'tuned' (Model D) background was available. Spectral products were generated using the HXDPINXBPI script provided by the *Suzaku* team, which includes a simulated contribution from the CXB using the form of Boldt (1987). As with the XIS detectors, we combined the individual spectra of sources with multiple observations into a single, averaged spectrum, and rebinned the data so that each energy bin had a minimum S/N of 3, lower than the minimum S/N required in the XIS spectra owing to the much lower PIN source rates, but still sufficient to allow the use of χ^2 minimization. Nominally we consider the PIN spectrum over the full 15–70 keV energy band, but in reality the exact energy range considered varies from source to source, depending on the highest energy at which each source is reliably detected.

[2] http://www.astro.isas.ac.jp/suzaku/analysis/hxd/

2.2 Sample selection

In this work, we are interested in 'bare' AGN, i.e. active galaxies with little or no intrinsic absorption, that display soft excesses. In order to identify such sources, we modelled the ∼2.5–10 keV energy range with a power-law continuum modified by Galactic absorption (see Table 1 for the Galactic neutral column densities adopted, as determined by Kalberla et al. 2005), modelled with the TBABS absorption code (Wilms, Allen & McCray 2000; the appropriate solar abundances for this model are used throughout); the iron K band (generally taken here as 4–7 keV) was excluded to prevent any iron emission present in the spectrum from influencing our continuum determination. We then extrapolated this continuum back through the 0.6–2.0 keV data and selected sources that displayed a clear and relatively smooth (i.e. not dominated by diffuse thermal emission, as is the case for e.g. NGC 1365; Wang et al. 2009) excess of emission over that predicted at lower energies. The resulting sample contains 25 sources that met our selection criteria; the observational details of these sources analysed are listed in Table 1. Note that this is largely based on a visual inspection of the spectra, so some of the sources selected may (and indeed do) display some mild, partially ionized absorption, but even in this minority of cases this absorption does not have a large effect on the observed spectrum.

3 SPECTRAL ANALYSIS

Here we detail our spectral analysis of the sample outlined in the previous section (see Table 1). In Section 3.1, we outline the basic approach we adopt for all the sources, and in Section 3.2 we provide additional, detailed information on a source-by-source basis. Spectral modelling is performed with XSPEC v12.6.0f (Arnaud 1996), and throughout this work the uncertainties quoted on model parameters are the 90 per cent confidence limits for one parameter of interest, unless stated otherwise. We also adopt as standard the cross-normalization constant of either $C_{\rm PIN/XIS0} = 1.16$ or 1.18 between the XIS0 and PIN spectra (the former for observations with the nominal pointing position centred on the XIS detectors, and the latter on the HXD detector), as recommended by the HXD calibration team.[3] However, since we are using combined FI XIS spectra in this work (XIS0, XIS2 and XIS3 where available), we take the extra step of comparing this with the XIS0 spectrum on a source-by-source basis in order to calculate the correct normalization constant for use between the combined XIS and PIN spectra, $C_{\rm PIN/XIS}$, using equation (1):

$$C_{\rm PIN/XIS} = C_{\rm XIS0/XIS} \times C_{\rm PIN/XIS0}\,. \quad (1)$$

We calculate $C_{\rm XIS0/XIS}$ by simultaneously modelling the combined FI XIS and XIS0 spectra with a phenomenological broken power-law model for the broad 0.6–10.0 keV continuum (excluding again the energy ranges 1.7–2.5 keV due to calibration uncertainties and 4.0–7.0 keV to exclude any iron emission), with all the physical parameters linked for the two spectra and only the normalization constant allowed to vary. The values of $C_{\rm PIN/XIS}$ we obtain are presented in Table 2. However, while this gives the appropriate normalization constant for the situation in which the PIN background is known perfectly, it does not account for any systematic uncertainties in the modelled background currently available, which are estimated by the HXD team to be 3 per cent;[4] therefore, we also investigate the consequences of allowing the XIS/PIN cross-normalization parameter to vary within the range equivalent to ±3 per cent of the background; these ranges and the values obtained are quoted in Table 3.

[3] http://www.astro.isas.jaxa.jp/suzaku/doc/suzakumemo/suzakumemo-2008-06.pdf

[4] http://heasarc.gsfc.nasa.gov/docs/suzaku/analysis/abc/

3.1 Basic approach

In this work, we are investigating the reflection-based interpretation for the broad-band X-ray spectra of active galaxies, i.e. that there are two main continuum components: a power-law-like component (PLC) most likely arising via electron scattering in some kind of corona, and a reflection-dominated component (RDC) arising due to irradiation of the disc by the PLC, which is modified by the strong gravitational effects present close to the black hole. This interpretation potentially provides a natural explanation in the form of the RDC for the soft excesses, broad iron lines and the hard excesses often displayed by AGN, and forms the basis of our spectral modelling. We try to take a broadly systematic approach, as detailed below, while also considering the specific details of each source individually, which are presented in Section 3.2, although, as the data quality declines so in general does the level of detail to which each source can be considered. The spectral complexities displayed by each source are highlighted in Fig. 1, in which we show the ratio of the XIS (black) and PIN (red) data to the absorbed power-law model discussed previously, using the cross-calibration normalizations calculated with equation (1).

Naturally, the PLC is modelled simply with a power-law emission component, with variable flux and photon index (Γ). To model the RDC component, we make use of the physically self-consistent reflection code REFLIONX (Ross & Fabian 2005). This model is specifically designed to account for the reprocessed emission from the cool, partially ionized accretion discs in AGN, intrinsically including both the reflected continuum and the imprinted atomic features, in particular the iron K-shell transitions. The key parameters of REFLIONX are the photon index of the ionizing continuum (assumed to be power-law-like) and the iron abundance ($A_{\rm Fe}$) and ionization state of the reflecting medium. The latter is quantified as the classic ionization parameter for a photoionized plasma, $\xi = L/nR^2$, where L is the ionizing luminosity, n is the number density of the reflecting medium and R is its distance from the primary X-ray source. Throughout this work, we require that the photon index of the ionizing continuum be that of the PLC, while the iron abundance and ionization parameter are free to vary (unless stated otherwise; see Section 3.2).

In order to account for the strong gravitational and Doppler effects that the emission from material orbiting close to the black hole will experience, we modify this reflected emission with RELCONV (Dauser et al. 2010), one of the most sophisticated relativistic convolution kernels. Under the assumption that the inner radius of the accretion disc is coincident with the ISCO, this kernel allows the black hole spin to be constrained directly from the RDC, and even allows for the intriguing possibility of black holes spinning in a retrograde sense with respect to the material orbiting in their accretion discs. The key free parameters of RELCONV are the spin of the black hole, the inclination of the disc (i) and the radial emissivity profile of the disc. We assume a single power-law emissivity profile for simplicity, i.e. $\epsilon(r) \propto r^{-q}$, where the emissivity index q is a free parameter. For a simple Newtonian 'lamp post' like geometry, in which the illuminating source is compact and centrally located, the predicted emissivity index is $q = 3$. However, this does not take into account any of the effects of general relativistic light bending, which focuses a larger fraction of the emission on to the inner disc if the X-ray

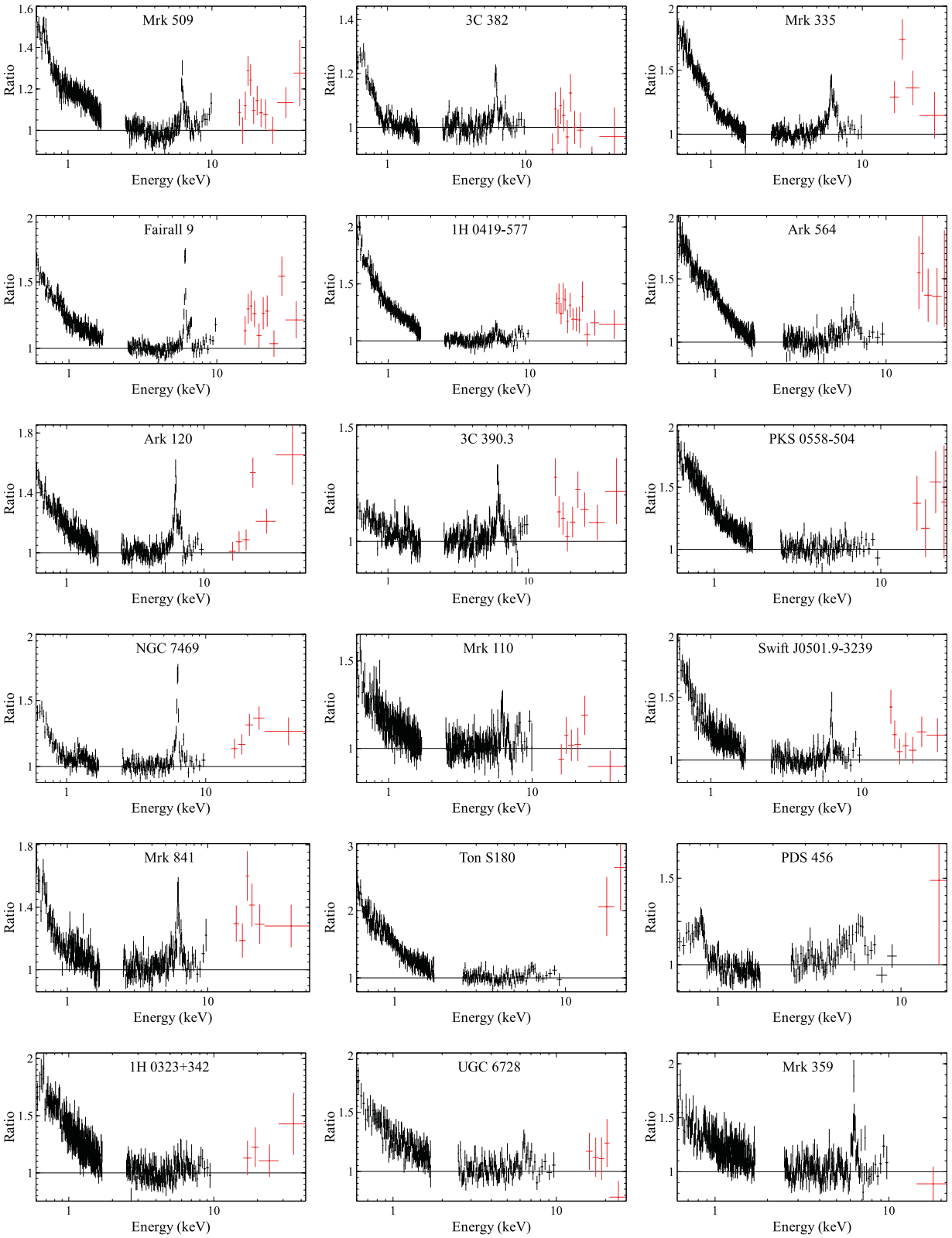

Figure 1. Data/model ratio plots of *Suzaku* XIS (front illuminated; black) and PIN (red) spectra to a power-law continuum model, as described in the text (Section 3.1), for the compiled sample. Each source displays a soft excess, and a number of sources also show evidence for broad iron emission components and/or for 'hard' excesses above ∼10 keV, although these features are by no means ubiquitous. The data shown have been rebinned for plotting purposes. Note that the photon indices of IRAS 13224−3809 and 1H 0707−495 have both been fixed at 2.7 (see Section 3.2). Furthermore, there are no robust PIN detections for either of these sources or for IRAS 05262+4432.

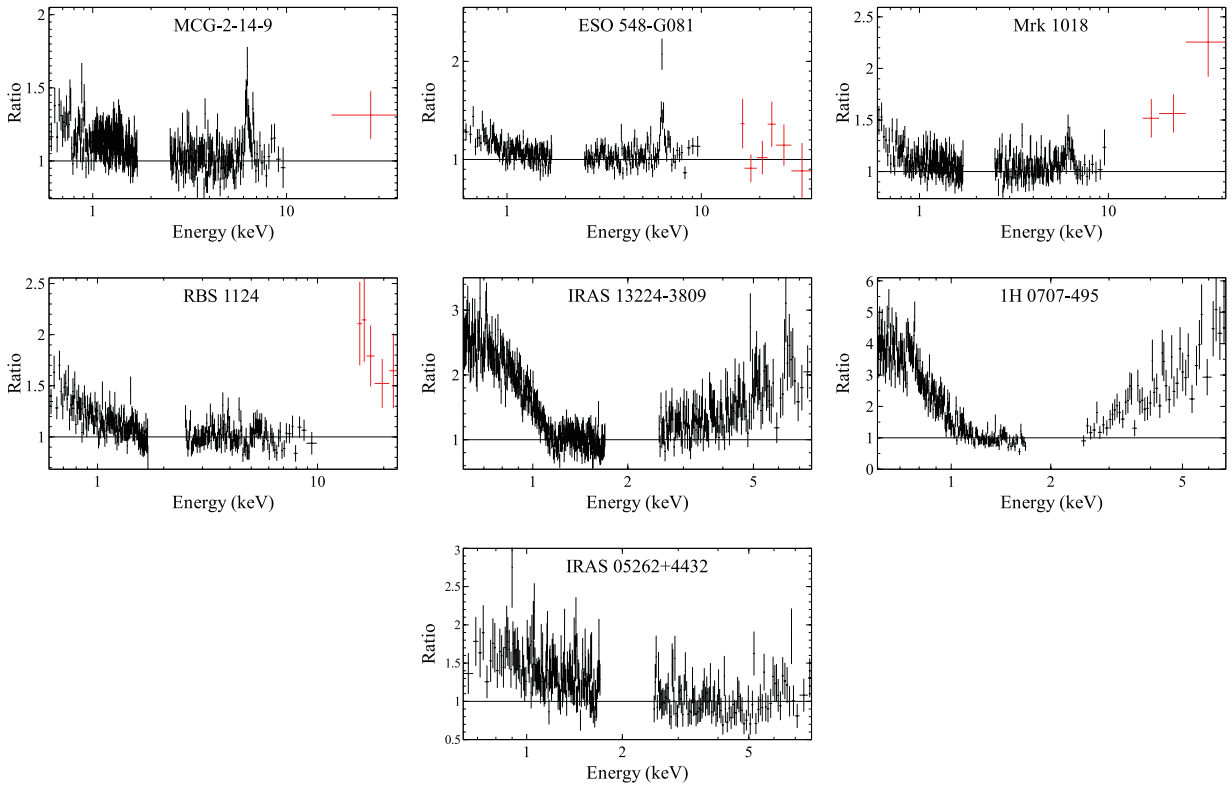

Figure 1 – *continued*

source is also located in a region of extreme gravity (Miniutti & Fabian 2004), or of relativistic time dilation. Both of these effects generally serve to steepen the inner emissivity profile (Wilkins & Fabian 2011); therefore, throughout this work we require that $q \geq 3$. The inner and outer radii of the disc are fixed, respectively, at the (spin-dependent) ISCO and at 400 $R_{\rm G}$ ($R_{\rm G} = GM/c^2$), the maximum value accepted by the model. It is also possible to include the effects of limb brightening/darkening, and we assume the latter following the calculations of Laor (1991).

With this RDC, we attempt to simultaneously account for the broad curvature across the 0.5–10.0 keV energy range that causes the appearance of a soft excess, any relativistically broadened iron emission detected and also any hard excess displayed by the AGN. However, this is a complex, multiparameter model component, and degeneracies can arise between various parameter combinations, particularly in the relativistic blurring parameters (see e.g. Nardini et al. 2011); this can be especially problematic with moderate quality data or when the features associated with reflection are weak. One of the main aims of this work is to provide where possible an initial, albeit model-dependent constraint on the black hole spin. Therefore, in cases where it is not possible to independently constrain all the blurring parameters, we fix, e.g., the inclination to 45° and/or the emissivity index to $q = 3$ in an attempt to provide at least a loose spin constraint. This was only necessary for the minority of cases (seven AGN in total) even including our analysis in which $C_{\rm PIN/XIS}$ was allowed to vary, although in four of these sources we were still unable to provide any constraint on the spin. Furthermore, in a few individual sources certain parameters might also be fixed for other reasons, e.g. the inclination being known a priori from radio constraints. Full details are provided in Section 3.2.

In addition to their broad-band continuum emission, active galaxies also very frequently display evidence for narrow emission features consistent with neutral iron (6.4 keV). Our general assumption is that these features also arise through reflection of the primary X-ray emission, but by cold, distant material rather than by the accretion disc, possibly associated with the torus-like structure that obscures the central X-ray sources of AGN viewed at high inclination angles. Therefore, where we see evidence for such a feature, our default procedure is to include a second, cold reflection component. This was also modelled with REFLIONX, with $\xi = 1.0$ (the lowest ionization state accepted by the model), while we required the iron abundance to be the same as that of the disc reflection component, and we again required that the photon index of the ionizing continuum to be the same as that of the PLC. This second reflector accounts for the narrow emission from neutral iron and, where present, may also contribute some emission to the hard excess. Less common than narrow emission from neutral iron, which is almost observed ubiquitously, AGN also sometimes display narrow emission features consistent with highly ionized iron (Fe XXV and Fe XXVI; 6.67 and 6.97 keV, respectively). Where we find evidence for these additional narrow features, we simply account for them with narrow ($\sigma = 10$ eV) Gaussian emission lines.

Finally, all emission components are modified by neutral absorption due to the Galactic interstellar medium. Again, we make use of the TBABS absorption code, and fix the column density at the Galactic value quoted in Table 1. Given that we have deliberately selected 'bare' active galaxies, we do not include any contribution from neutral absorption intrinsic to the source. However, despite our source selection method, high-resolution grating spectra of some of the sources included in this work do show evidence for some weak, partially ionized absorption intrinsic to the source. Where this is the case, we include an ionized absorber using the XSTAR photoionization code (Kallman & Bautista 2001) to account for the main features in our lower resolution CCD spectra. The free parameters of the

Table 2. Key parameters obtained for the reflection-based models constructed for the compiled sample (see Section 3.2 for details). Parameters in parentheses have not been allowed to vary, and where we were unable to constrain the black hole spin this is indicated with a 'U'.

Source	En. range (keV)	$C_{\rm PIN/XIS}$	Γ	$A_{\rm Fe}$ (solar)	ξ (erg cm s^{-1})	q	i (°)	a^*	χ^2_ν (χ^2/d.o.f.)
Mrk 509	0.6–44.0	1.17	2.04 ± 0.01	0.5 ± 0.1	170^{+30}_{-80}	>7.4	<18	$0.86^{+0.02}_{-0.01}$	1314/1333
3C 382	0.6–53.0	1.14	1.81 ± 0.01	>5.1	500^{+60}_{-240}	>6.1	(40)	$0.75^{+0.07}_{-0.04}$	1366/1317
Mrk 335	0.6–36.0	1.17	2.16 ± 0.01	1.4 ± 0.2	220 ± 10	>4.9	50^{+8}_{-7}	$0.83^{+0.10}_{-0.13}$	1233/1152
Fairall 9	0.6–39.0	1.16	1.99 ± 0.01	1.1 ± 0.2	140^{+60}_{-30}	>3.5	45^{+13}_{-9}	>0.64	1276/1253
1H 0419−577	0.6–48.0	1.19	$1.98^{+0.01}_{-0.02}$	0.9 ± 0.1	104^{+4}_{-26}	$5.4^{+0.2}_{-1.0}$	51^{+4}_{-6}	>0.88	1384/1294
Ark 564	0.6–22.0	1.20	2.52 ± 0.01	$1.0^{+0.2}_{-0.1}$	540^{+40}_{-20}	>6.2	64^{+1}_{-11}	$0.96^{+0.01}_{-0.06}$	1081/1011
Ark 120	0.6–53.0	1.22	2.13 ± 0.01	2.7 ± 0.6	9^{+2}_{-4}	$7.0^{+2.7}_{-2.2}$	54^{+6}_{-5}	$0.81^{+0.10}_{-0.18}$	1316/1177
3C 390.3	0.6–49.0	1.16	1.66 ± 0.01	$3.1^{+1.2}_{-0.5}$	840^{+490}_{-220}	(3)	(35)	U	1302/1259
PKS 0558−504	0.6–24.0	1.13	$2.30^{+0.02}_{-0.01}$	$0.9^{+0.3}_{-0.1}$	270^{+70}_{-30}	4.0 ± 0.7	(45)	>0.80	990/1022
NGC 7469	0.6–52.0	1.19	$1.84^{+0.03}_{-0.02}$	$2.9^{+1.7}_{-1.0}$	200^{+20}_{-50}	>4.6	<54	>0.96	1262/1139
Mrk 110	0.6–45.0	1.19	$1.96^{+0.02}_{-0.01}$	0.7 ± 0.2	310^{+220}_{-80}	>7.4	31^{+4}_{-6}	>0.99	1184/1115
Swift J0501.9−3239	0.6–36.0	1.22	$2.06^{+0.04}_{-0.03}$	$1.8^{+0.9}_{-0.5}$	200^{+10}_{-40}	>5.1	<48	>0.96	1025/1056
Mrk 841	0.6–53.0	1.19	$1.85^{+0.03}_{-0.01}$	1.0 ± 0.2	210^{+20}_{-70}	$4.1^{+2.8}_{-1.9}$	45^{+7}_{-5}	>0.56	1089/1053
Ton S180	0.6–23.0	1.16	2.36 ± 0.01	$0.9^{+0.2}_{-0.1}$	280^{+50}_{-20}	>8.1	60^{+3}_{-1}	$0.91^{+0.02}_{-0.09}$	876/838
PDS 456	0.6–17.0	1.15	$2.30^{+0.03}_{-0.01}$	>8.4	59^{+17}_{-4}	$5.9^{+1.8}_{-1.5}$	70^{+3}_{-5}	>0.97	829/826
1H 0323+342	0.6–42.0	1.25	$1.91^{+0.03}_{-0.01}$	0.8 ± 0.2	250^{+40}_{-20}	(3)	(45)	>0.48	864/922
UGC 6728	0.6–26.0	1.27	$2.00^{+0.04}_{-0.03}$	$0.7^{+0.6}_{-0.3}$	190^{+80}_{-170}	$6.8^{+2.8}_{-1.4}$	<55	>0.95	877/885
Mrk 359	0.6–21.0	1.15	$1.89^{+0.04}_{-0.03}$	$1.5^{+0.9}_{-0.6}$	21^{+32}_{-16}	>4.1	47 ± 6	$0.66^{+0.30}_{-0.46}$	820/833
MCG−2-14-9	0.6–37.0	1.19	1.89 ± 0.02	(1)	<10	(3)	(45)	U	802/804
ESO 548-G081	0.6–36.0	1.23	1.70 ± 0.03	$3.5^{+4.1}_{-1.5}$	570^{+560}_{-380}	(3)	(45)	U	853/845
Mrk 1018	0.6–41.0	1.21	$1.94^{+0.04}_{-0.03}$	$2.0^{+1.4}_{-0.7}$	5^{+10}_{-4}	>3.9	45^{+14}_{-10}	$0.57^{+0.31}_{-0.82}$	681/721
RBS 1124	0.6–23.0	1.22	$1.86^{+0.04}_{-0.02}$	$2.9^{+1.5}_{-0.9}$	51^{+7}_{-9}	>8.4	66^{+5}_{-15}	>0.98	661/668
IRAS 13224−3809	0.6–7.6	–	(2.7)	(20)	22 ± 3	$6.1^{+0.7}_{-0.6}$	(64)	>0.995	447/412
1H 0707−495	0.6–6.7	–	(2.7)	(10)	53^{+1}_{-2}	$7.6^{+0.4}_{-0.3}$	(58)	>0.994	278/236
IRAS 05262+4432	0.6–7.8	–	$2.18^{+0.13}_{-0.06}$	(1)	<51	(3)	(45)	U	234/231

absorption model used here are the ionization state (again quantified as ξ), the column density and the line-of-sight velocity of the absorbing medium; the abundances of the absorbing medium are assumed to be solar, and its turbulent velocity is fixed at 200 km s^{-1}. In addition, there has been growing evidence for AGN displaying highly blueshifted absorption features from highly ionized iron (see e.g. Tombesi et al. 2010), typically interpreted as evidence for rapid outflows (although see Gallo & Fabian 2011, for an alternative explanation). Where we find evidence for similar features, we also treat these with XSTAR, although in these cases we will use grids specifically designed to treat absorption by highly ionized material, as detailed below.

3.2 Individual source details

Here, we provide further information specific to our individual modelling of each source, including details on any additional emission or absorption features included beyond the basic PLC+RDC interpretation. The key reflection parameters obtained from our spectral modelling are quoted in Table 2 ($C_{\rm PIN/XIS}$ fixed at the values obtained from equation 1) and in Table 3 ($C_{\rm PIN/XIS}$ free to vary within the range defined by the 3 per cent systematic uncertainty on the modelled PIN background). We also show 1D confidence contours of the spin parameter for the full range considered for each source in Fig. 2, based where possible on the results presented in Table 3. Note that these contours have been generated with the inclination limited to $i \leq 75°$ for sources in which this parameter is free to vary.

Mrk 509. In addition to the basic PLC+RDC interpretation for the continuum, we also include a moderately ionized absorber at the redshift of the host galaxy, with $\log \xi = 2.03 \pm 0.04$ erg cm s^{-1} and $N_{\rm H} = 1.9^{+0.4}_{-0.5} \times 10^{21}$ atom cm^{-2}. The ionization obtained is consistent with that of the most prominent absorbing zone found in the detailed RGS analysis presented by Detmers et al. (2011) as part of the substantial multiwavelength observing campaign recently carried out on this source (see also Kaastra et al. 2011), but the column obtained here is larger. This may be due to our simplistic, single-zone treatment of the absorber, but the inclusion of a second ionized absorbing zone does not offer a substantial improvement. We also find a narrow emission feature consistent with neutral iron, so include a distant reflector, and additional emission consistent with an Fe XXV. The latter is modelled with a narrow Gaussian emission component, and we find an equivalent width of $\rm EW_{XXV} = 17^{+9}_{-10}$ eV; the inclusion of this feature provides an improvement of $\Delta\chi^2 = 23$ for an additional degree of freedom. Here, we find that the normalization between the XIS and PIN spectra plays an important role in determining the interplay between the PLC and RDC continuum components, and hence in determining the reflection parameters. When $C_{\rm PIN/XIS}$ is allowed to vary the inclination obtained is significantly larger, although still reasonable for an unobscured AGN, and the spin is lower and less constrained. Furthermore, the ionization of the absorber increases to $\log \xi = 2.38^{+0.08}_{-0.13}$ erg cm s^{-1}.

Table 3. Key parameters obtained for the reflection-based models constructed for the compiled sample when $C_{\rm PIN/XIS}$ was free to vary within the indicated range. Again, parameters in parentheses have not been allowed to vary, and where we were unable to constrain the black hole spin this is indicated with a 'U'.

Source	$C_{\rm PIN/XIS}$ (range)	Γ	$A_{\rm Fe}$ (solar)	ξ (erg cm s^{-1})	q	i (°)	a^*	χ^2_ν (χ^2/d.o.f.)
Mrk 509	<1.06 (1.04–1.30)	1.99 ± 0.01	0.5 ± 0.1	13^{+8}_{-5}	>4.3	50^{+5}_{-3}	$0.36^{+0.20}_{-0.37}$	1302/1332
3C 382	<1.03 (0.99–1.29)	1.82 ± 0.01	$1.7^{+0.4}_{-0.3}$	200^{+10}_{-70}	(3)	(40)	<0.81	1358/1317
Mrk 335	1.19 ± 0.11 (0.79–1.55)	2.16 ± 0.01	1.4 ± 0.2	220 ± 10	>4.9	50^{+8}_{-9}	$0.83^{+0.09}_{-0.13}$	1233/1151
Fairall 9	1.06 ± 0.06 (0.95–1.37)	2.00 ± 0.01	$0.9^{+0.2}_{-0.1}$	130^{+70}_{-30}	$5.2^{+4.5}_{-1.4}$	44^{+13}_{-9}	$0.82^{+0.09}_{-0.19}$	1269/1252
1H 0419−577	$1.27^{+0.06}_{-0.05}$ (0.93–1.45)	$1.97^{+0.03}_{-0.01}$	0.8 ± 0.1	120^{+10}_{-20}	$5.2^{+0.3}_{-1.3}$	49^{+7}_{-4}	>0.89	1380/1293
Ark 564	$1.40^{+0.17}_{-0.18}$ (0.79–1.61)	2.53 ± 0.01	$1.0^{+0.2}_{-0.1}$	550^{+40}_{-30}	>6.0	64^{+1}_{-11}	$0.96^{+0.01}_{-0.07}$	1078/1010
Ark 120	<1.04 (1.00–1.43)	2.14 ± 0.01	$1.8^{+0.2}_{-0.3}$	6^{+5}_{-2}	$5.1^{+2.8}_{-1.1}$	47^{+7}_{-2}	$0.64^{+0.19}_{-0.11}$	1274/1176
3C 390.3	$1.21^{+0.05}_{-0.04}$ (1.01–1.31)	1.65 ± 0.01	$4.5^{+1.7}_{-1.9}$	1060^{+360}_{-350}	(3)	(35)	U	1301/1258
PKS 0558−504	>1.23 (0.70–1.56)	$2.30^{+0.02}_{-0.01}$	$1.0^{+0.3}_{-0.2}$	270^{+90}_{-30}	4.1 ± 0.7	(45)	>0.95	985/1021
NGC 7469	<1.13 (1.01–1.37)	$1.81^{+0.02}_{-0.01}$	$1.1^{+0.5}_{-0.2}$	200^{+20}_{-100}	>5.5	(45)	$0.64^{+0.13}_{-0.20}$	1261/1139
Mrk 110	<1.07 (0.96–1.42)	$1.92^{+0.01}_{-0.02}$	$0.7^{+0.2}_{-0.1}$	250^{+230}_{-40}	>5.4	<43	$0.96^{+0.03}_{-0.07}$	1179/1114
Swift J0501.9−3239	>1.25 (1.07–1.37)	2.09 ± 0.04	$3.1^{+1.4}_{-1.2}$	200^{+10}_{-70}	$9.0^{+0.4}_{-2.7}$	32^{+10}_{-28}	>0.99	1019/1055
Mrk 841	$1.14^{+0.08}_{-0.10}$ (0.90–1.48)	1.86 ± 0.02	$0.9^{+0.3}_{-0.2}$	190^{+30}_{-110}	$4.1^{+2.8}_{-1.9}$	46^{+6}_{-5}	>0.52	1088/1052
Ton S180	>1.46 (0.42–1.90)	2.36 ± 0.01	$0.9^{+0.2}_{-0.1}$	280^{+30}_{-20}	>8.3	60^{+3}_{-1}	$0.92^{+0.03}_{-0.11}$	869/837
PDS 456	$1.34^{+0.77}_{-0.72}$ (0.00–2.97)	$2.30^{+0.03}_{-0.01}$	>8.5	59^{+16}_{-8}	$5.9^{+2.2}_{-1.8}$	70^{+3}_{-6}	>0.96	829/825
1H 0323+342	>1.26 (0.89–1.61)	$1.92^{+0.01}_{-0.02}$	$0.8^{+0.3}_{-0.2}$	260^{+40}_{-30}	(3)	(45)	>0.37	861/921
UGC 6728	<1.41 (1.02–1.52)	$1.98^{+0.14}_{-0.12}$	$0.8^{+0.8}_{-0.4}$	<500	>4.5	(45)	>0.71	877/884
Mrk 359	$0.78^{+0.24}_{-0.23}$ (0.33–1.97)	1.90 ± 0.03	$1.2^{+0.7}_{-0.4}$	21^{+32}_{-17}	>4.1	47^{+10}_{-8}	$0.66^{+0.30}_{-0.54}$	814/832
MCG−2-14-9	$1.19^{+0.26}_{-0.23}$ (0.54–1.85)	1.89 ± 0.02	(1)	<26	(3)	(45)	U	802/803
ESO 548-G081	<1.21 (0.98–1.48)	$1.71^{+0.05}_{-0.02}$	$2.2^{+1.8}_{-1.1}$	270^{+520}_{-160}	(3)	(45)	U	850/844
Mrk 1018	>1.27 (0.94–1.48)	$1.93^{+0.03}_{-0.04}$	$2.7^{+1.7}_{-1.2}$	7^{+18}_{-5}	>3.4	46 ± 9	$0.58^{+0.36}_{-0.74}$	676/720
RBS 1124	>1.46 (0.84–1.60)	1.86 ± 0.05	$2.7^{+1.8}_{-0.9}$	50^{+10}_{-40}	>6.9	64^{+7}_{-13}	>0.97	649/667

3C 382. As one of the few broad-line radio galaxies (BLRGs) included in this sample, it is possible to obtain an independent constraint on the inclination at which the source is viewed at from radio observations of its jet, assuming that the jet axis is aligned perpendicular to the plane of the inner disc. Although it is difficult to rigorously test this assumption, we note that the Galactic binary system XTE J1550−564, one of the few cases in which it has been possible to independently constrain the orbit and jet inclinations, appears to be consistent with this picture (Steiner & McClintock 2012). Therefore, when applying the PLC+RDC continuum, we fixed the inclination at $i = 40^\circ$, consistent with the radio constraint presented by Giovannini et al. (2001).

In addition to this underlying continuum, there is also a narrow feature associated with neutral iron and, as initially reported by Sambruna et al. (2011), evidence for a further narrow feature at ∼7.5 keV. We include a distant reflector to account for the former, and the latter is modelled with a narrow Gaussian emission line. The inclusion of this Gaussian results in an improvement of $\Delta\chi^2 = 19$ for two additional degrees of freedom, and we find a (rest-frame) line energy of $E_{\rm G} = 7.53 \pm 0.04$ keV and an equivalent width of $\rm EW_G = 19 \pm 9$ eV; the energy of this feature precludes an association with iron, but is consistent with moderately ionized nickel. Finally, we also include a moderately ionized absorber at the redshift of the galaxy, similar to that found by Torresi et al. (2010) in their analysis of the high-resolution *XMM–Newton* RGS spectrum of this source, with $\log\xi = 2.5 \pm 0.1$ erg cm s^{-1} and $N_{\rm H} = 1.4^{+0.7}_{-0.5} \times 10^{21}$ atom cm^{-2}. As with Mrk 509, the normalization between the XIS and PIN spectra plays an important role in determining the interplay between the PLC and RDC continuum components in this case, and hence in constraining the reflection parameters. We find that when $C_{\rm PIN/XIS}$ is allowed to vary the iron abundance obtained is much lower, and the spin and the emissivity index are essentially unconstrained. Therefore, in Table 3 we present the results obtained with the index fixed at the Newtonian prediction ($q = 3$), although the spin is still only very weakly constrained.

Mrk 335. In addition to the basic PLC+RDC model adopted in this work, we also see evidence for narrow emission features consistent with neutral iron and Fe XXV, similar to Patrick et al. (2011b). The former is modelled with a distant reflector, and the latter is simply modelled with narrow ($\sigma = 10$ eV) Gaussian line profile. The inclusion of the latter feature provides a strong improvement of $\Delta\chi^2 = 33$ for one extra degree of freedom, although it does not significantly affect the parameters obtained for the main PLC and RDC continuum components, and we find an equivalent width of $\rm EW_{XXV} = 29 \pm 9$ eV. The spin obtained here is very similar to that presented by Patrick et al. (2011b) for the same data set, and is consistent with both the spin inferred from the inner radius obtained by Grupe et al. (2008) in their analysis of the low-flux *XMM–Newton* data sets and the spin measured from the recent intermediate-flux *XMM–Newton* observations by Gallo et al. (2012).

Fairall 9. In addition to the standard PLC+RDC continuum considered here, we also detect strong, narrow emission features consistent Fe I and Fe XXVI, and a weaker emission feature consistent with Fe XXV. A distant reflector is included to model the former, and

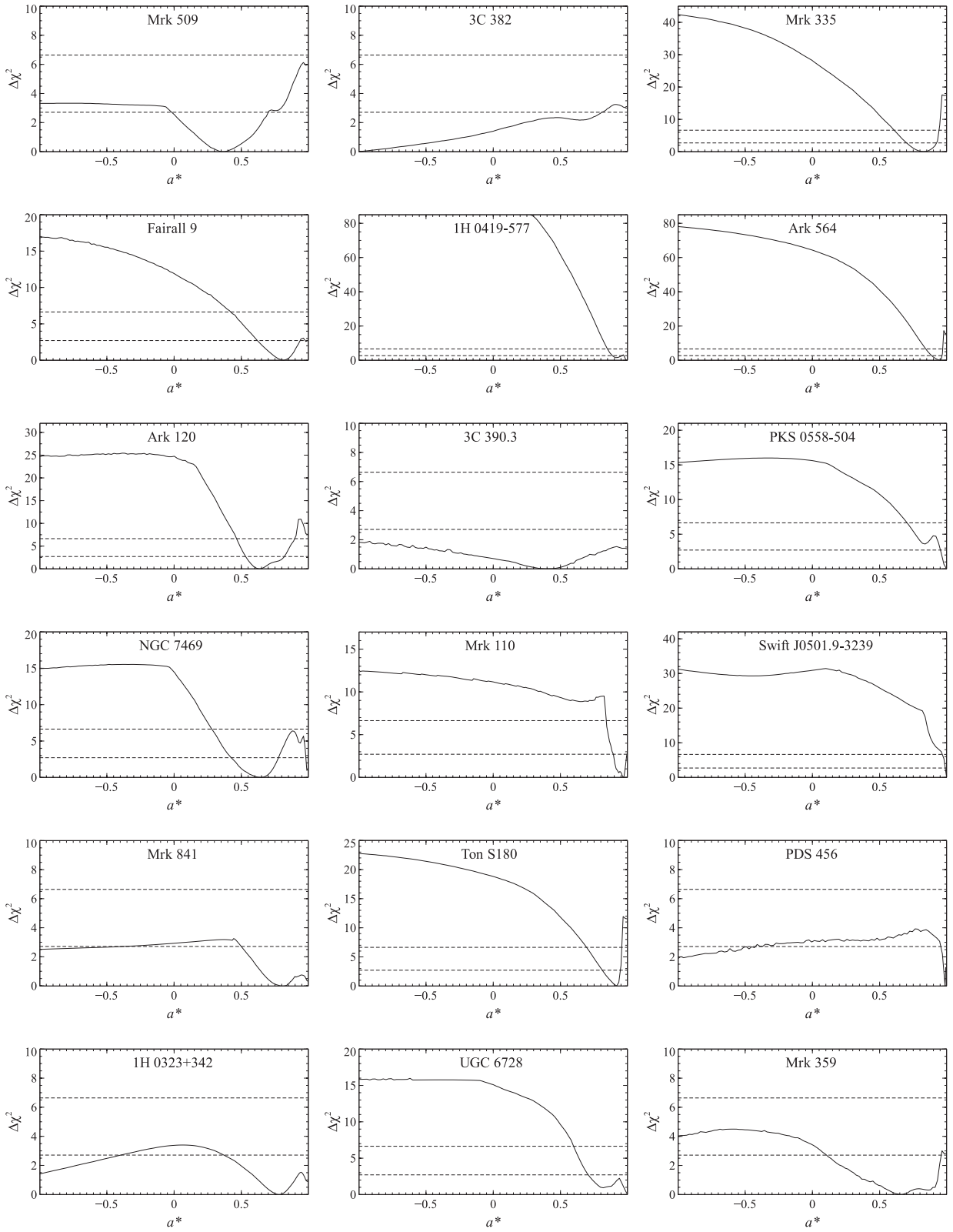

Figure 2. χ^2 confidence contours for the spin measurements obtained for the compiled sample, based (where possible) on the results obtained when allowing $C_{\rm XIS/PIN}$ to vary (see Table 3). Horizontal dashed lines represent $\Delta\chi^2$ equivalent to the 90 and 99 confidence intervals.

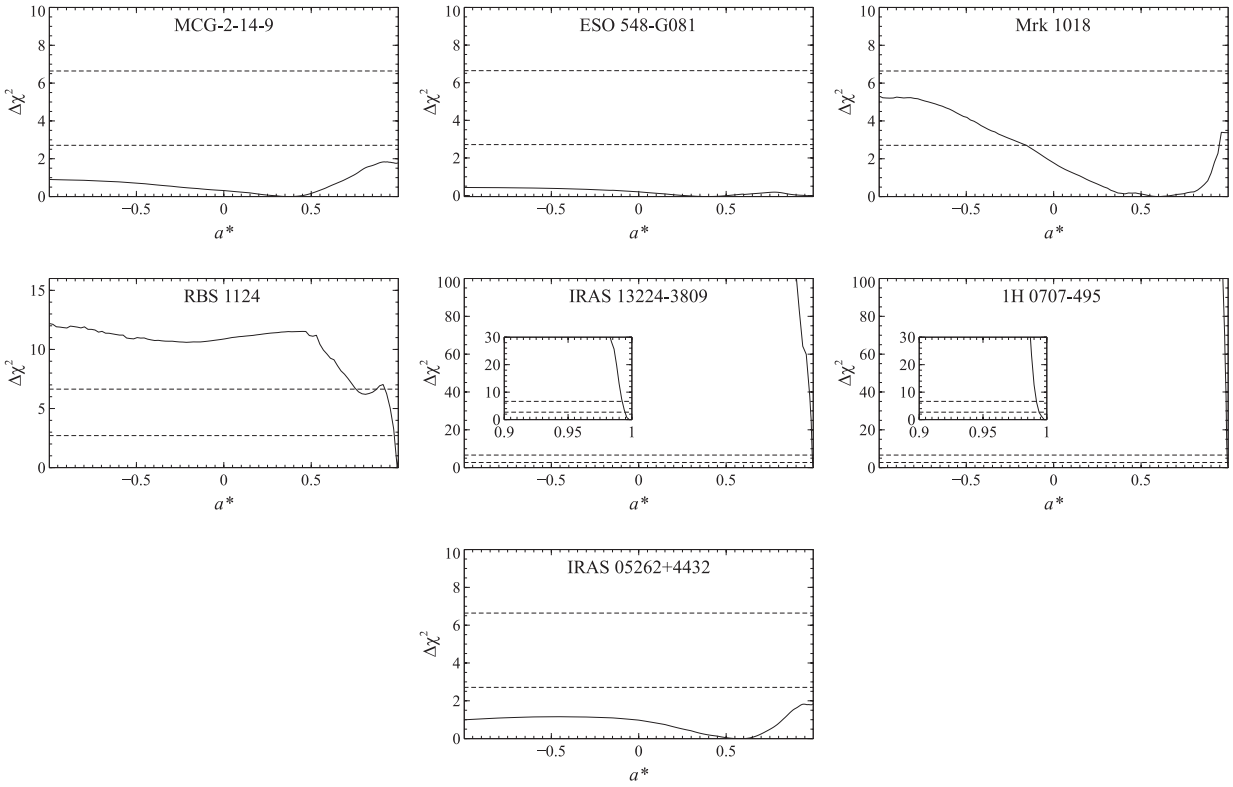

Figure 2 – *continued*

the latter two are modelled with narrow ($\sigma = 10$ eV) Gaussian line profiles. The equivalent widths obtained are $\mathrm{EW_{XXV}} = 13^{+7}_{-5}$ eV and $\mathrm{EW_{XXVI}} = 35^{+8}_{-7}$ eV for the ionized emission lines and their inclusion results in respective improvements of $\Delta\chi^2 = 14$ and 52 for one extra degree of freedom in each case. Although the inclusion of the Fe XXVI feature does have a significant effect on some of the main reflection parameters, the best-fitting model excluding this line resulted in an estimate for the inclination of 87°, which is unphysically high for an unobscured AGN. Conversely, the inclusion of the Fe XXV line does not significantly modify the key parameters further. The spin obtained here is larger, although still consistent with those obtained by Schmoll et al. (2009) with the same data set, by Patrick et al. (2011a) with a later *Suzaku* observation not included here (performed after 2010 October) and by Emmanoulopoulos et al. (2011a) with a long *XMM–Newton* observation, but is lower than that presented in Patrick et al. (2011b) again with the same data set.

1H 0419−577. In addition to the PLC+RDC components, we also detect a weak narrow emission feature consistent with neutral iron, and therefore include a second, distant reflector. The spin constraint obtained here is consistent with that inferred both in our previous work on the first *Suzaku* data set (Walton, Reis & Fabian 2010) and in the *XMM–Newton* analysis of Fabian et al. (2005).

Ark 564. The basic PLC+RDC interpretation provides a good fit to the data. No narrow iron emission or absorption lines are detected. The spin obtained here is consistent with that inferred from the inner radius obtained by Dewangan et al. (2007), who modelled the long 2005 *XMM–Newton* observation with blurred reflection.

Ark 120. In addition to the basic PLC+RDC continuum, we also detect a narrow emission feature consistent with neutral iron, and hence include a second, distant reflector. The spin obtained here is broadly similar to, although slightly better constrained than, that obtained by Nardini et al. (2011) with the emissivity index fixed at $q = 5$, but is lower than that obtained by Patrick et al. (2011b) with the same data set.

3C 390.3. Similar to 3C 382, 3C 390.3 is a BLRG, and hence we fix the inclination at $i = 35°$ when applying the PLC+RDC continuum, consistent with the radio constraint on the inclination presented by Giovannini et al. (2001). In addition to this underlying continuum, we find evidence for a strong narrow emission feature consistent with neutral iron, and hence include a distant reflector. However, owing to the weak features associated with reflection, we are unable to reliably constrain all the parameters of interest, and even when fixing the emissivity index at $q = 3$ we find the spin to be unconstrained. Note that similar to Sambruna et al. (2009) we also include an unresolved Gaussian component at ∼1.4 keV to account for a feature in the background spectrum.

PKS 0558−504. Here the basic PLC+RDC interpretation provides a good fit to the data; no statistically compelling narrow iron emission lines are detected. However, when free we find that the inclination obtained is very high ($i \gtrsim 75°$), unphysically high for an unobscured active galaxy. This is most likely due to the complex parameter degeneracies that can arise when using multiparameter reflection models (see e.g. Nardini et al. 2011). Therefore, we instead present the results obtained with the inclination fixed at 45°, similar to the rough estimation of Gliozzi et al. (2010) based on the radio morphology of the source.

NGC 7469. In addition to the PLC+RDC continuum, there is a strong narrow emission line consistent with neutral iron, so we again include a distant cold reflector. We also include a weak, moderately ionized absorber at the redshift of the galaxy, based on the most prominent absorption component detected by Blustin et al. (2007) when modelling the high-resolution *XMM–Newton* RGS spectrum. As the absorber has an extremely weak effect on the spectrum in

this case, we only allow the column to vary, fixing the ionization parameter at $\log \xi = 2.73$, and find $N_{\rm H} = 1.7^{+1.2}_{-0.8} \times 10^{21}$ atom cm^{-2}, consistent with that obtained previously. In this case, when allowing $C_{\rm PIN/XIS}$ to vary it is not possible to constrain all the reflection parameters of interest, so we present the results with the inclination fixed at 45°. In addition to the global minimum presented in Table 3, there is a further, local minimum with a very high spin ($a^* \gtrsim 0.98$) which also satisfies $\Delta\chi^2 < 2.71$ (see Fig. 3), equivalent to the best fit obtained with $C_{\rm PIN/XIS}$ fixed presented in Table 2.

Mrk 110. In addition to the PLC+RDC continuum, we also detect a strong narrow emission feature consistent with neutral iron, and a possible narrow absorption feature at ∼7.5 keV. We include a distant reflector to account for the former, and model the latter with a highly ionized photoionized plasma using the XSTAR code. The absorption zone here is assumed to have solar abundances and a turbulent velocity of ∼1000 km s^{-1}, while the column, ionization parameter and outflow velocity are free to vary, and we find $N_{\rm H} = 9.6^{+0.7}_{-7.2} \times 10^{22}$ atom cm^{-2}, $\log \xi = 4.2 \pm 0.3$ and $v_{\rm out} = 0.079 \pm 0.005c$. The inclusion of this absorber provides an improvement of $\Delta\chi^2 = 21$ for three extra degrees of freedom.

Swift J0501.9−3239. In addition to the basic PLC+RDC continuum, we also detect a narrow emission feature consistent with neutral iron, and include a second, distant reflector.

Mrk 841. In addition to the PLC+RDC components, we also detect a narrow emission feature consistent with neutral iron and therefore include a contribution from a second, distant reflector. We also include a moderately ionized absorber at the redshift of the galaxy similar to the most prominent absorption component detected by Longinotti et al. (2010) in their analysis of the high-resolution *XMM–Newton* RGS spectrum of this source, with $\log \xi = 2.2 \pm 0.2$ erg cm s^{-1} and $N_{\rm H} = 2.1^{+0.9}_{-0.8} \times 10^{21}$ atom cm^{-2}. Although we present the prograde spin solution in Tables 2 and 3, there is also a local minimum with retrograde spin ($a^* \lesssim -0.4$) that also just about satisfies $\Delta\chi^2 < 2.71$ (see Fig. 2). The prograde solution is consistent with the inner radii obtained by Petrucci et al. (2007) in their analysis of the available *XMM–Newton* data.

Ton S180. The basic PLC+RDC continuum provides a good fit to the data, no narrow emission or absorption lines are detected over the energy range considered. The spin constraint obtained here is very similar to that presented by Nardini et al. (2012), who kept the inclination fixed at 45°.

PDS 456. In addition to the PLC+RDC continuum, there is also well-documented evidence for absorption due to an extremely high velocity outflow (Reeves et al. 2009). Owing to the high iron abundance obtained, we follow our original approach and model the outflow with a photoionized plasma with a variable iron abundance, fixed to that of the reflector for consistency. The other abundances are assumed to be solar, and the turbulent velocity is assumed to be ∼3000 km s^{-1} following Reeves et al. (2009). The column, ionization parameter and outflow velocity are allowed to vary, and we find $N_{\rm H} = 7^{+2}_{-3} \times 10^{21}$ atom cm^{-2} and $\log \xi = 3.52^{+0.35}_{-0.03}$, consistent with our previous work, and $v_{\rm out} = 0.31 \pm 0.01c$, consistent with Reeves et al. (2009). As discussed in Walton et al. (2010), the high iron abundance and in particular the high inclination obtained here are driven by the association of the emission feature at ∼0.8 keV with reflected iron L-shell emission, as opposed to arising due to complex parameter degeneracies as is likely to be the case for PKS 0558−504, so in this instance we consider the values obtained to be robust. As with Mrk 841, there is also a local minimum with a retrograde spin ($a^* \lesssim -0.5$) that satisfies $\Delta\chi^2 < 2.71$ (see Fig. 3). However, the prograde solution obtained is consistent with our previous work on this data set. Note finally that in this case, in order to include a PIN detection, it was necessary to relax our rebinning requirement to an S/N of 2 instead of 3.

1H 0323+342. In this case, the basic PLC+RDC interpretation provides a good fit to the data; no statistically compelling narrow iron emission lines are detected. However, similar to the earlier case of PKS 0558−504, when free we find that the inclination obtained is unphysically high for an unobscured active galaxy ($i = 82° \pm 3°$). Therefore, we again present the results obtained with the inclination fixed at 45°. However, we are still not able to constrain all the reflection parameters of interest, so we present the results obtained assuming $q = 3$. Note that when $C_{\rm PIN/XIS}$ is free to vary, in addition to the prograde solution presented in Table 3, there is also a local minimum with a retrograde spin ($a^* \lesssim -0.4$) which also satisfies $\Delta\chi^2 < 2.71$ (see Fig. 2), similar to Mrk 841.

UGC 6728. In addition to the underlying PLC+RDC continuum, we also detect a narrow emission feature consistent with neutral iron, and hence include a second, distant reflector. Here, as for NGC 7469, when allowing $C_{\rm PIN/XIS}$ to vary we were not able to reliably constrain all the reflection parameters of interest, so we present the results with the inclination fixed at 45°.

Mrk 359. In addition to the basic PLC+RDC continuum, we also detect a narrow emission feature consistent with neutral iron, and hence include a second, distant reflector. We also include an unresolved Gaussian component at ∼5.9 keV to account for a feature in the background spectrum. The formal global minimum gives a solution in $i > 85°$ and the spin is unconstrained. However, as with PKS 0558−504 and 1H 0323+342, we consider this to be unphysically high for an unobscured source, and there is a local minimum of essentially equal statistical quality with $i \sim 45°$, so we instead present this solution. The spin is only weakly constrained.

MCG−2-14-9. In addition to the PLC+RDC continuum, we also detect a narrow emission feature consistent with neutral iron, and hence include a second, distant reflector. A very good fit is obtained; however, in this case, owing to the moderate data quality and the relatively weak reflection features, even when fixing the inclination at 45°, the iron abundance at the solar value, and the emissivity index at the Newtonian prediction ($q = 3$), we are unable to provide a preliminary spin constraint.

ESO 548-G081. In addition to the basic PLC+RDC continuum, we also detect a strong narrow emission feature consistent with neutral iron, and include a second, distant reflector. As with MCG−2-14-9, a very good fit is obtained, but owing to the moderate data quality and the relatively weak reflection features, even fixing the inclination at 45°, and the emissivity index at the Newtonian prediction, we are unable to provide a preliminary spin constraint.

Mrk 1018. In this case, the PLC+RDC continuum provides an excellent fit, no statistically compelling narrow lines are detected. However, the spin is only very weakly constrained.

RBS 1124. Here, the basic PLC+RDC continuum also provides a good fit to the available data. The spin constraint for this data set initially presented by Miniutti et al. (2010) is broadly consistent with that obtained here.

IRAS 13224−3809. In this case, the XIS data quality is fairly poor, only extending up to ∼7.6 keV, and even relaxing our binning constraint to an S/N of 2 we do not obtain a robust PIN detection. However, we have recently undertaken a long observing campaign on this source with *XMM–Newton*, in which the source is found to display a sharp, deep drop above ∼7.5 keV which is not well detected here owing to the poor data quality (see Fabian et al. 2012a, and also Boller et al. 2003; Ponti et al. 2010). This feature, as well as the spectrum at higher energies, is extremely important in determining the iron abundance, inclination and also the photon index, so

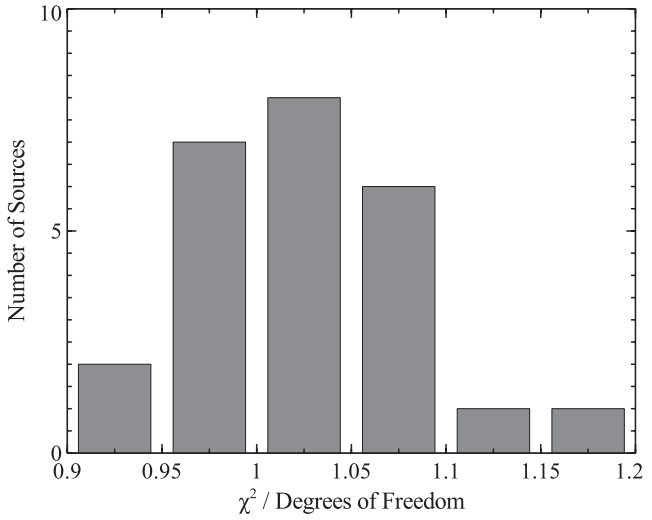

Figure 3. The number distribution of reduced χ^2 values obtained with our PLC+RDC interpretations for the presented sample of AGN.

in this case we take these values from our *XMM–Newton* analysis. Furthermore, to remain consistent with this more detailed analysis, we also include a low temperature ($kT = 0.106 \pm 0.005$ keV) blackbody component, which may also be associated with irradiation of the accretion disc. In addition, we also include an unresolved Gaussian at ∼5.9 keV to account for a feature in the background spectrum.

Owing to the extreme nature of this source, by fixing the above parameters we still obtain a very strong spin constraint despite the relatively poor data quality, which is consistent with the inner radius originally obtained by Ponti et al. (2010) and the spin obtained with our long *XMM–Newton* exposure (Fabian et al. 2012a). This remains the case even when the key parameters informed by our *XMM–Newton* analysis are allowed to vary within their quoted uncertainties. If we allow instead for a dual-ionization reflector ($\xi_1 = 20^{+1}_{-7}$, $\xi_2 = 490^{+50}_{-200}$ erg cm s^{-1}), as proposed in Fabian et al. (2012a), the fit improves to $\chi^2_\nu = 417/410$, but the spin constraint obtained does not change. Attempts to fit lower spins, while still imposing the same limits on the other key parameters, result in the model significantly underpredicting the data at high energies. Removing the constraint on the photon index results in $\Gamma = 2.22^{+0.06}_{-0.05}$ and a substantially weaker constraint on the spin, $a^* > 0.9$, although this is still constrained to be high. If the constraints on the iron abundance and the disc inclination are also removed, the model becomes too degenerate to reliably constrain the spin solely using the *Suzaku* data, even if the blackbody component is also removed, and the values obtained for these quantities are substantially different from those obtained with the significantly higher quality *XMM–Newton* data ($A_{\rm Fe}$/solar $= 5^{+2}_{-1}$, $i = 30^\circ \pm 4^\circ$), despite not being expected to evolve with time. Furthermore, we stress that neither of these cases with relaxed parameter constraints correctly include the sharp high-energy drop known to be present in this source. Therefore, we will proceed with the model in which the photon index, iron abundance and disc inclination are fixed at the values obtained with *XMM–Newton*.

1H 0707−495. Again, the XIS data quality here is rather poor, the source only being detected up to ∼6.7 keV, and there is no robust PIN detection. As with IRAS 13224−3809, this source is well documented as having a deep, sharp drop above ∼7 keV (Boller et al. 2002; Fabian et al. 2004, 2009, 2012b; Gallo et al. 2004; Zoghbi et al. 2010), which is not detected owing to the poor data quality, leading to the same problems in determining the iron abundance, disc inclination and photon index. The spectrum obtained with this *Suzaku* observation is fairly reminiscent of the most recent *XMM–Newton* observation, presented in Fabian et al. (2012b), so we adopt the photon index of 2.7 obtained in that work. We also fix the inclination and the iron abundance values at those obtained in the more detailed studies presented by Zoghbi et al. (2010), Fabian et al. (2012b) and most recently Kara et al. (2012).

As with IRAS 13324−3809, by fixing these key parameters to their previously obtained values we are still able to obtain a strong spin constraint despite the poor data quality, owing again to the extreme nature of this source. The spin obtained here is consistent with that originally presented in Fabian et al. (2009) and also that found in subsequent reflection-based analyses (see also Dauser et al. 2012). Again, allowing the key parameters informed by the higher quality *XMM–Newton* data to vary within their quoted uncertainties does not significantly affect the spin constraint obtained, nor does adopting a dual-ionization reflector ($\xi_1 < 41$, $\xi_2 = 130^{+110}_{-60}$ erg cm s^{-1}) similar to that proposed in Fabian et al. (2012b), despite the latter modification providing a moderate improvement in the quality of fit ($\chi^2_\nu = 264/234$). Attempts to force lower spin values with the same constraints on the other key parameters result in severe underestimation of the data at higher energies. In fact, this source was caught in such a reflection-dominated state (see Section 4.2) that, even removing the constraints on the photon index, iron abundance and disc inclination, the spin is still constrained to be high ($a^* > 0.88$). However, the values obtained for the iron abundance and disc inclination ($A_{\rm Fe}$/solar $= 3.4^{+1.2}_{-0.8}$, $i = 40^{\circ}{}^{+3^\circ}_{-10^\circ}$), which should not vary with time, are highly discrepant with those obtained from any high-quality *XMM–Newton* observation, and as with IRAS 13224−3809 the sharp high-energy drop known to be present disappears from the model. We therefore again proceed with the model in which the parameters are fixed based on previous *XMM–Newton* analysis.

IRAS 05262+4432. Here, the XIS data quality is extremely poor, only extending up to ∼7.8 keV, and as with IRAS 13224−3809 and 1H 0707−495 there is no robust PIN detection. A good fit is obtained with the basic PLC+RDC interpretation, but even when fixing the inclination at 45°, the iron abundance at the solar value and the emissivity index at the Newtonian prediction, we are unable to provide a preliminary spin constraint.

4 DISCUSSION

We have presented a spectral analysis of a sample of 25 'bare' active galaxies observed with the *Suzaku* satellite. These are sources that display either no intrinsic absorption or only very weak intrinsic absorption, and have been selected on the basis of the presence of a relatively smooth soft excess below ∼2 keV after extrapolation of the ∼2–10 keV continuum to lower energies. Owing to this lack of absorption, such sources offer the best opportunity to study the intrinsic emission spectra of active galaxies. In addition to the soft excesses required for selection, a number of the sources also show evidence for broad iron emission components (e.g. Mrk 335, Fairall 9, Ark 564; see Fig. 1) and/or for 'hard' excesses above ∼10 keV in the PIN data, although these features are not ubiquitous within the presented sample.

Our analysis is based around interpreting these spectral complexities as reflected emission from the accretion disc. For each source, we have constructed a continuum model consisting of a PLC, associated with Compton upscattering in an X-ray-emitting corona, and an RDC arising through irradiation of the surface of the

accretion disc by the Comptonized emission. The reflected emission has been modelled with the physically self-consistent reflection code REFLIONX (Ross & Fabian 2005), which treats both the backscattered continuum emission and the atomic features produced when optically thick material is irradiated by a power-law-like X-ray continuum, and the relativistic effects relevant for emission from an accretion disc in the strong gravity regime close to a black hole are included with the RELCONV convolution kernel (Dauser et al. 2010). In addition to their continuum emission, many of the AGN analysed also display narrow emission lines consistent with neutral iron, which we associate with reflection from cold, distant material, and treat with a second, unmodified REFLIONX component. A small minority also show evidence for discrete emission lines associated with highly ionized iron (Fe XXV and/or Fe XXVI), which we model with simple Gaussian emission line profiles. All the emission components are modified by neutral, Galactic absorption. Finally, a further minority also show evidence for some minor absorption, either at low energies from moderately ionized material or at high energies from highly ionized material. Where present, we have modelled this absorption with the XSTAR photoionization code (Kallman & Bautista 2001). In this work, we have attempted to simultaneously combine a systematic approach to analysing the sample as a whole, with a detailed physical treatment of each individual source (see Section 3.2).

In all the cases analysed, we have been able to successfully model the available broad-band spectra with a reflection-based interpretation; Fig. 3 shows the distribution of the values obtained for the reduced χ^2 ($\chi^2_\nu = \chi^2$/d.o.f.) with our PLC+RDC based interpretations for the analysed sample. This distribution clearly displays a fairly narrow peak around $\chi^2_\nu = 1$. This demonstration of the flexibility of disc reflection is important, as we have previously argued in Walton et al. (2012) that this process is a fundamental consequence of the widely accepted disc–corona accretion geometry.

4.1 Sample properties

Having successfully modelled the observed data, we now consider the results obtained for some of the physical properties of the accretion flow for the compiled sample, focusing conservatively on the results obtained with $C_{\rm XIS/PIN}$ allowed to vary (Table 3). In general, when they could be constrained, the disc inclinations obtained from our analysis are either moderate or low, as would be expected for a sample selected on the basis of a lack of obscuration.[5] For a couple of the AGN considered, the formal best fit does return unphysically high inclinations when this parameter is left free to vary given the nature of the selected sources. However, we attribute this to the complex dependencies and degeneracies that can arise between the various parameters in such a complex, multiparameter model, which can be especially problematic when modelling data of only moderate quality and/or a relatively featureless spectrum. Crucially, we are still able to obtain acceptable solutions in these cases even when fixing the inclination at a physically more reasonable value (45°).

It may at first seem surprising that the majority of inclinations obtained are moderate (∼50°) rather than low (≲30°). However, there are two factors that result in a natural bias towards higher inclinations (up to the point that sources are excluded due to obscuration by the torus, above ∼70°). We have already mentioned that

[5] Recall that the probability distribution for the inclination of randomly orientated disc-like sources follows $P(i) \propto \sin(i)$.

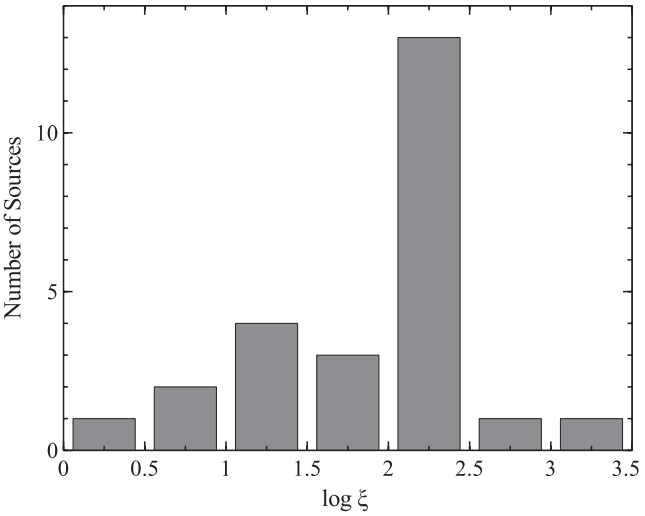

Figure 4. The number distribution obtained for the logarithm of the ionization parameter of the reflecting medium with our PLC+RDC based interpretations.

for disc-like structures, $P(i) \propto \sin(i)$, so we naturally expect there to be more AGN with high inclinations. In addition, the majority of sources analysed appear to require high spin (see Section 4.3). For such sources, the reflected flux observed in the soft X-ray bandpass is greater at high inclinations than low inclinations, owing to the larger line-of-sight velocities of the material in the disc at high inclinations. This results in an enhancement of the reflected flux observed owing to the additional special relativistic beaming along angles close to the plane of the disc, and also in additional reflected flux being blueshifted into the soft X-ray bandpass. The combined strength of these effects depends on both the spin of the black hole and the emissivity profile; for a maximally rotating black hole with a steep ($q = 6$) emissivity, the reflected flux at soft energies for a source observed at $i = 80°$ can be more than a factor of ∼2 larger than that for the same source observed at $i = 10°$, while for a non-rotating black hole with an emissivity of $q = 3$ the reflected flux in the soft band appears practically isotropic. Therefore, by basing our sample selection on the presence of a soft excess, we are probably introducing an additional bias towards higher inclination sources, since rapid spins are generally inferred.

In terms of the ionization state of the reflecting medium (i.e. the surface of the disc), as shown in Fig. 4, we find a fairly broad range of ionization parameters, ranging from ∼10 to 1000 erg cm s^{-1}. The vast majority of sources are found to have $\xi \lesssim 400$, suggesting that, as expected, iron is very rarely highly ionized in AGN. There is a fairly strong peak in the obtained distribution around $\xi \sim 300$, corresponding to iron being primarily found in its Fe XIX–Fe XXI ions (Kallman et al. 2004). At these ionization states, resonant trapping and Auger destruction of the Kα photons are expected to be very efficient, and the emitted iron line should only be very weak (Matt, Fabian & Ross 1993; Ross, Fabian & Brandt 1996). This offers a natural explanation as to why a number of the sources do not show any strong evidence for relativistically broadened iron emission (see Fig. 1).

In Fig. 5, we also plot the number distribution of the best-fitting iron abundances obtained; only sources for which we were able to constrain this quantity are included. The distribution clearly peaks around a solar iron abundance, with the vast majority of sources consistent with having an abundance within a factor of ∼2 of this

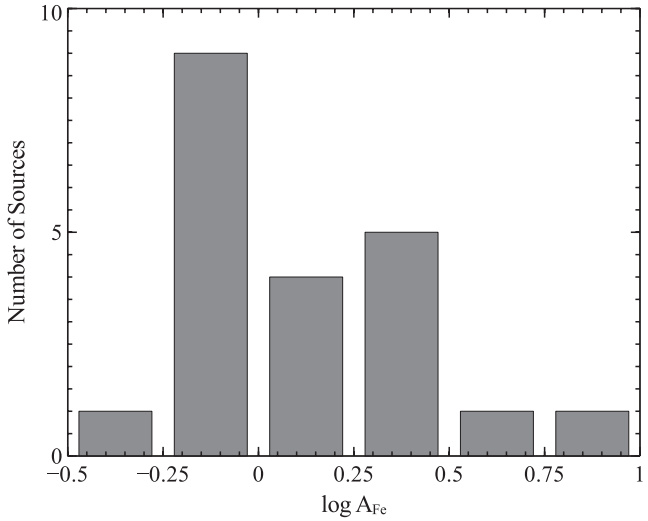

Figure 5. The number distribution obtained for the logarithm of the iron abundance of the reflecting medium with our PLC+RDC based analysis.

value. This is similar to the preference for a roughly solar abundance reported by Crummy et al. (2006) in their earlier application of disc reflection to a general sample of AGN, despite the two samples only sharing five sources in common. Our analysis results in a substantially supersolar iron abundance for only one source, PDS 456 (although highly supersolar iron abundances are also adopted for 1H 0707−495 and IRAS 13224−3809, this is based on prior analyses rather than being constrained by the data analysed here). As discussed previously, this is driven by the association of the emission feature observed at ∼0.9 keV with iron L-shell emission in the reflected contribution.

4.2 Reflection strength

A further quantity of interest is the implied strength of the reflected emission from the disc relative to the intrinsic PLC emission, $R_{\rm disc}$, which can provide information on the geometry of the accretion flow. In order to estimate $R_{\rm disc}$, in a manner consistent with the literature, we make brief use of the PEXRIV Compton reflection code (Magdziarz & Zdziarski 1995), in which R is directly included as a free parameter. R is normalized such that a reflecting medium subtending a solid angle of $\Omega = 2\pi$, as seen by the illuminating source, gives a value of $R = 1$. The other key parameters of this model are the photon index and the high-energy cut-off of the ionizing continuum, and the inclination, abundances and ionization of the reflecting medium. However, as PEXRIV does not self-consistently include any fluorescent atomic emission, which can be of significant importance in determining the reflected flux at soft energies, we estimate $R_{\rm disc}$ from the strength of the Compton reflection hump in our best-fitting models, rather than applying PEXRIV to the data directly, as follows.

To remain consistent with our detailed modelling, the photon index, disc inclination, iron abundance and ionization parameter are all set to the best-fitting values presented previously, and to remain consistent with the manner in which the REFLIONX model was computed, the high-energy cut-off was set to 300 keV and the other elemental abundances were set to their solar values. The normalization of the PEXRIV component was then set such that when $R_{\rm disc}$ is set to zero the 2–10 keV flux matches that of the PLC component. Finally, $R_{\rm disc}$ is determined such that the 15–50 keV flux matches that of the combined PLC+RDC components in the rest frame, i.e. once the relativistic effects applied by RELCONV have been removed. We repeat this process for the best-fitting models obtained both when $C_{\rm PIN/XIS}$ was fixed and when it was free to vary, and the results obtained are given in Table 4. As we are not directly applying PEXRIV to the data, we do not estimate any statistical uncertainties on the values obtained for $R_{\rm disc}$, and stress that these should only be considered as approximate estimates given the nature in which they are determined.

Table 4. Approximate estimates for the relative strength of the reflected emission from the accretion disc, based on the strength of the best-fitting Compton reflection hump (see text).

Source	$R_{\rm disc}$	
	$C_{\rm PIN/XIS}$ fixed	$C_{\rm PIN/XIS}$ free
Mrk 509	0.7	0.5
3C 382	0.05	0.1
Mrk 335	0.8	0.8
Fairall 9	0.4	0.4
1H 0419−577	1.5	1.3
Ark 564	1.5	1.5
Ark 120	1.6	1.5
3C 390.3	0.03	0.03
PKS 0558−504	1.0	1.0
NGC 7469	0.8	0.2
Mrk 110	2.6	1.2
Swift J0501.9−3239	2.1	3.7
Mrk 841	0.3	0.3
Ton S180	1.4	1.4
PDS 456	1.2	1.2
1H 0323+342	0.5	0.5
UGC 6728	1.5	1.4
Mrk 359	1.0	1.0
MCG−2-14-9	0.3	0.3
ESO 548-G081	0.1	0.1
Mrk 1018	1.3	1.2
RBS 1124	3.3	2.9
IRAS 13224−3809	16	–
1H 0707−495	275	–
IRAS 05262+4432	1.3	–

In Fig. 6, we show the distribution of the values for $R_{\rm disc}$ obtained, where possible, when $C_{\rm PIN/XIS}$ was free to vary. This distribution shows a clear peak around $R_{\rm disc} \sim 1$ (the median value is ∼1.2), as broadly expected for a central isotropic emission source illuminating a geometrically thin accretion disc. However, there are also some specific individual results worth drawing attention to. First of all, the reflection fraction inferred for 1H 0707−495 is *extremely* large. This is consistent with our previous assertion that the *Suzaku* data are reminiscent of the *XMM–Newton* observation obtained recently in 2011, which caught 1H 0707−495 in an almost completely reflection-dominated state (see Fabian et al. 2012b). The reflection fraction obtained for IRAS 13224−3809 is also large, consistent with that estimated from our recent long *XMM–Newton* observation (Fabian et al. 2012a). At the other end of the scale, it is interesting to note that both of the radio-loud AGN included in the compiled sample display extremely weak reflection features. This would be expected if the illuminating X-ray corona were associated with the base of the jet, as suggested by Markoff, Nowak & Wilms (2005) (see also Beloborodov 1999). It would be of great interest to further test this scenario by investigating whether systematically weak

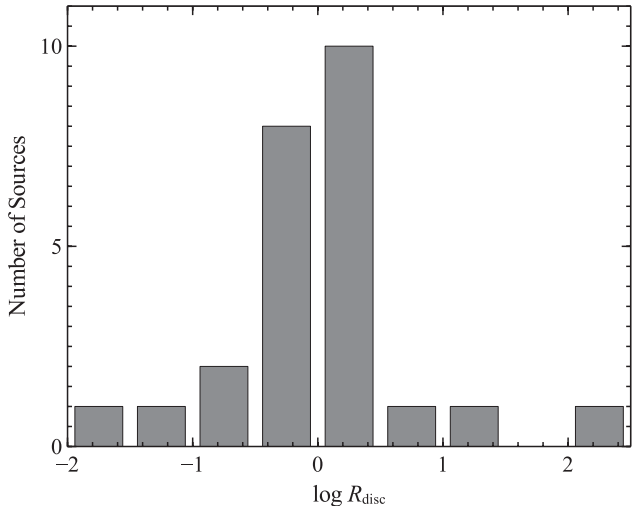

Figure 6. The number distribution obtained for $\log R_{\rm disc}$ estimated from our best-fitting PLC+RDC continuum models.

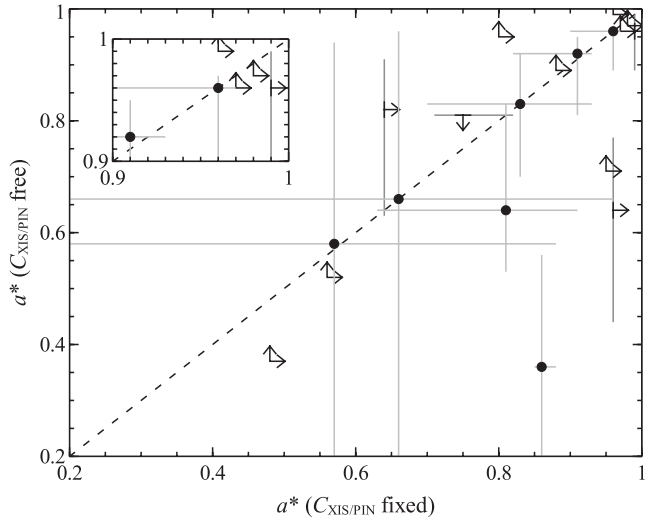

Figure 7. A comparison of the spin constraints obtained with $C_{\rm XIS/PIN}$ fixed and with $C_{\rm XIS/PIN}$ free to vary. Where limits are obtained, these are indicated with arrows. In many cases, allowing $C_{\rm XIS/PIN}$ to vary does not significantly change the spin constraint obtained, although as discussed in Section 3.2 there are some notable exceptions.

reflection features are a general trait of radio-loud AGN with a much larger sample of such sources.

4.3 Black hole spin

In addition to generally testing the robustness of the disc reflection interpretation, during the course of this analysis we have endeavoured to use the inferred contribution from the reflected emission to place initial constraints on the black hole spin, although this has not always been possible, and it should be noted that the constraints presented are model dependent. Where the spin could be well constrained, rapid prograde spins are generally obtained, although the black holes are certainly not always inferred to be maximally rotating. Even when the spin is only relatively loosely constrained, some kind of rotation is generally implied. There are no sources that are strongly constrained to be Schwarzschild black holes, although there are a few sources that remain consistent with this interpretation. There are also no sources that are strongly constrained to have a retrograde spin, although again there are a few sources that remain consistent with this scenario. Therefore, if relativistic disc reflection is responsible for the intrinsic spectral complexities displayed by AGN, and as discussed previously there is very good evidence to suggest that this is the case, the implication is that the majority of AGN may be rotating fairly rapidly. Where the spin has been successfully measured via reflection for other sources not included in this work, the results obtained also seem to be consistent with this picture (Brenneman & Reynolds 2006; Brenneman et al. 2011; Cowperthwaite & Reynolds 2012; Reis et al. 2012; note that in the latter case, although the favoured spin implies a retrograde rotation with respect to the material in the disc, the black hole is still inferred to be rapidly rotating). For the majority of the sources analysed, where a measurement of either the spin or the inner radius of the disc has been made previously, either using one of the same data sets analysed here or a different observation obtained at some other epoch, the spin obtained here is consistent with the previous work, although there are some notable exceptions highlighted in Section 3.2. Where it has not been possible to reliably constrain the spin, this has largely been due to either a data quality issue or a lack of strong reflection features.

In this work, we have carefully attempted to determine the correct cross-normalization constant to use between the combined XIS and PIN spectra based on the recommendations of the *Suzaku* HXD calibration team. To do so, we have first compared the combined XIS spectrum with the single XIS0 spectrum, and used this comparison to calculate the normalization constant $C_{\rm XIS/PIN}$ from the normalization constants obtained by the *Suzaku* team between the XIS0 and PIN detectors using equation (1). In general, we find a good agreement between the combined XIS and XIS0 spectra, as would be expected, although in rare cases the normalizations of these spectra can be discrepant by up to ∼8 per cent (see UGC 6728). We have also investigated what effect allowing this value to vary has on the results obtained, as it does not account for any systematic uncertainties on the level of the modelled instrument background. These are estimated to be ∼3 per cent, and so we have allowed $C_{\rm XIS/PIN}$ to vary within an appropriate range based on this uncertainty. The results obtained allowing $C_{\rm XIS/PIN}$ to vary in this manner are quoted in Table 3. Focusing on the spin parameters, doing so does not appear to have any single systematic effect on the results obtained, in terms of either the preferred value or its statistical uncertainty. As demonstrated in Fig. 7, allowing $C_{\rm XIS/PIN}$ to vary has little or no effect on the spin obtained in many cases, even when the PIN spectrum carries some significant statistical weight (e.g. Mrk 841), while in some the spin becomes more tightly constrained (e.g. PKS 0558−504), and in others it becomes substantially more difficult to constrain (e.g. Mrk 509). However, the general conclusions drawn above still seem to be robust.

We now consider the fractional distribution of the results shown in Fig. 2 for the black hole spins of the compiled sample. Here, we again only consider sources for which the data quality and/or the strength of the reflected features were sufficient to allow at least some constraint to be placed on the spin at the 90 per cent confidence level. However, in many cases the statistical uncertainties obtained are non-Gaussian and cover a broad range of spin values, which can be significantly larger than any desirable bin size for such a distribution. As a compilation of AGN spin is one of the primary goals of this work, we take a more careful approach and

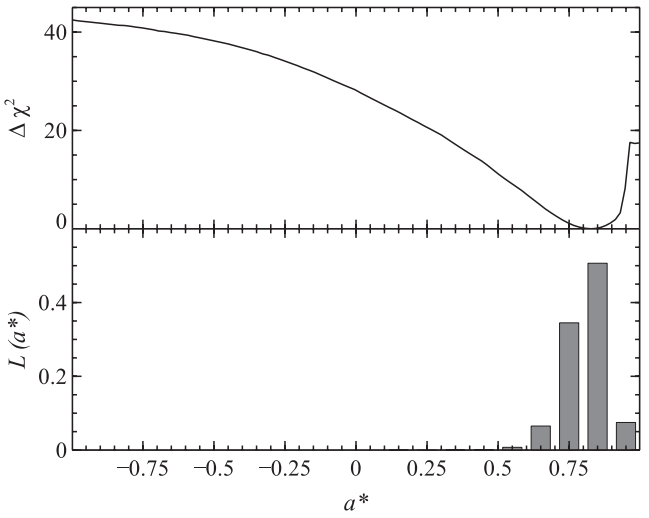

Figure 8. The likelihood distribution obtained for the spin parameter for Mrk 335 (bottom panel) from the χ^2 confidence contour (top panel); each bin spans a range of $\Delta a^* = 0.1$.

attempt to account for these uncertainties when plotting the distribution of spins we obtain. We do so by combining the likelihood distributions[6] for the spin parameters, $L(a^*)$, of the sample rather than simply the best-fitting values. These distributions are derived from the χ^2 confidence contours displayed in Fig. 2, assuming that $L(a^*) \propto \exp(-\Delta\chi^2/2)$ and is normalized such that the sum of the likelihoods over the $-0.998 \leq a^* \leq 0.998$ range considered here is unity. As an example, in Fig. 8 we show the likelihood distribution obtained from the χ^2 contour for Mrk 335. Finally, the individual likelihood distributions are then combined and renormalized again to form a composite likelihood distribution for the compiled sample. The distribution obtained, shown in Fig. 9, clearly displays a strong peak at higher spin values. This is consistent with the typically small inner radii obtained by Crummy et al. (2006).

As discussed previously, the spin of the SMBHs powering AGN is widely expected to be determined by their growth history. Over the lifetime of these nuclear black holes, galaxy mergers and prolonged accretion can impart enough angular momentum to determine the spin distribution of AGN in the current epoch. Berti & Volonteri (2008) calculated the local spin distributions expected for various different SMBH growth scenarios under the assumption that the SMBH seeds were not rotating. When SMBH growth is dominated solely by mergers, i.e. galaxy mergers resulting in the coalescence of the two central SMBHs, the expected spins appear to be fairly randomly distributed, with a slight peak at low spin owing to their assumption regarding the initial seeds. However, prolonged accretion is found to be the dominant mechanism in determining the expected distribution of AGN spins. When the accretion is ordered, the central black holes are generally spun up, leading to a strong preference for rapidly rotating black holes. If instead the accretion is chaotic, i.e. the angular momenta of the accreted material and the AGN are not typically aligned, the AGN will experience the opposite effect and be spun down, leading to a strong preference for slowly rotating black holes. Therefore, measuring the spin for a large sample of AGN has important implications regarding the nature in which their black holes grow. Our observational analysis suggests a preference for at least some rotation, and probably for rapid rotation, which if taken at face value is most consistent with the scenario in which SMBH growth is dominated by ordered accretion.

However, before drawing any firm conclusions, we must first consider whether the general high spin preference obtained here is likely to be representative of the true underlying spin distribution. Brenneman et al. (2011) suggest there may actually be an observational bias towards AGN with high spin, based on the widely held expectation that the radiative efficiency of accretion on to a black hole increases with black hole spin, which should result in AGN with high spin being brighter on average than their low spin counterparts. Based on this, Reynolds et al. (2012) estimate that for a flux-limited sample drawn from an AGN population with a flat intrinsic spin distribution, only ∼30 per cent of the sources in the sample would have a spin of $a^* < 0.5$, despite the true value being 50 per cent. Furthermore, as demonstrated in Appendix A, we find that it is easier to statistically constrain higher spins, which is probably a natural consequence of the form of the relation between black hole spin and the radius of the ISCO (see Bardeen, Press & Teukolsky 1972). Given our method for compiling the sample likelihood distribution, this may also introduce some slight bias towards higher spins. Nevertheless, where we have been able to constrain the spin well at the 90 per cent confidence level, rapid rotation (i.e. $a^* > 0.5$) is almost always required, and this subset of the sample compiled is large enough that even given this probable observational bias we might have expected to find at least one source that is constrained to have low spin if the intrinsic distribution does not truly peak at higher spins. However, we stress that the sample presented is certainly not a complete, flux-limited sample, so the picture that appears to be growing could yet change.

A further important consequence of our analysis, independent of the presence of any potential biases, regards the radio-loud/radio-quiet AGN dichotomy. It has previously been suggested that the observational differences between these classes of AGN are due to differences in the spins of the black holes powering these sources (Blandford 1990; Wilson & Colbert 1995; Moderski, Sikora & Lasota 1998; Garofalo, Evans & Sambruna 2010). In this picture, radio-loud AGN host black holes with high spin that can launch powerful jets via magnetic extraction of the rotational energy of the black hole, as proposed by Blandford & Znajek (1977), while radio-quiet AGN have low spin and cannot launch jets via this method. However, our analysis implies that, if the PLC+RDC interpretation adopted here is correct, then this cannot be the case, as the majority of AGN included in this work are radio quiet, yet are found to have high spin. This is not to say that the process outlined by Blandford & Znajek (1977) is not present at all; when jets are present they may well carry more power for AGN with high spin than for AGN with low spin. However, black hole spin would not be sufficient by itself to solely determine jet production in AGN. This is similar to the observed behaviour of Galactic BHBs, where the presence of jets appears to be determined by the accretion state of the black hole (see e.g. Fender, Belloni & Gallo 2004); the same BHB can be observed both with and without jets at different epochs, despite the fact that its spin cannot have evolved substantially. Black hole spin may yet prove to be important for certain jet properties, but it does not appear to play a substantial role in determining whether jets are produced in the first place.

Although we have presented the largest compilation of AGN spins to date, in order to build a more robust picture the number of sources with reliable spin measurements must still be increased.

[6] These distributions are designed to represent the underlying probability distributions for the spin parameters given the available data, but as this is not a fully Bayesian analysis they cannot formally be classed as such.

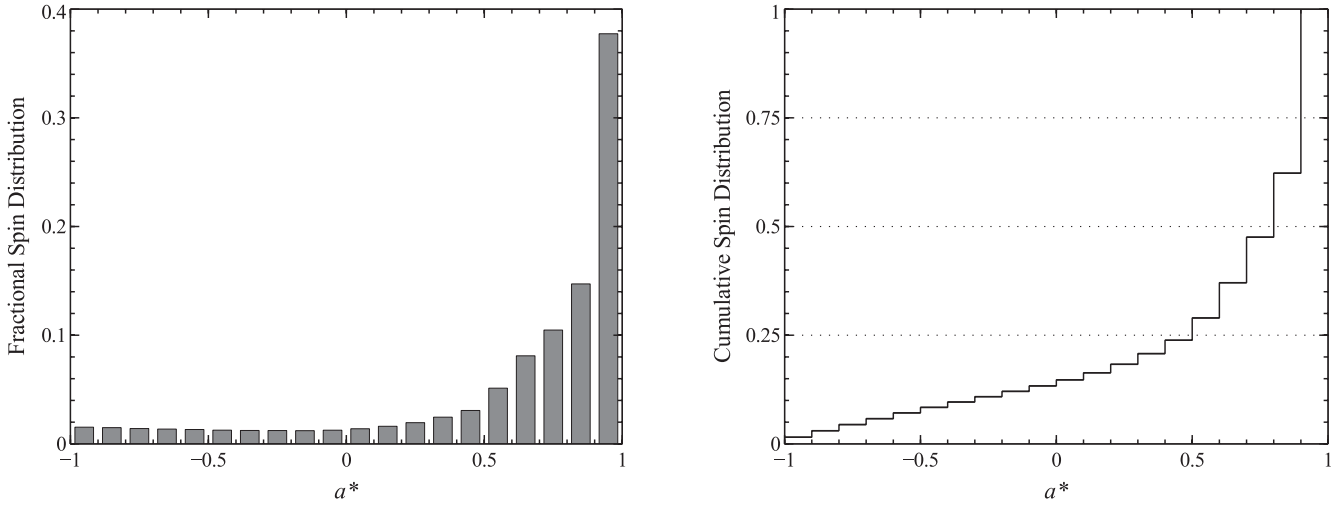

Figure 9. Fractional (left-hand panel) and cumulative (right-hand panel) distributions for the black hole spins obtained for the compiled sample of AGN (see text); each bin spans a range of $\Delta a^* = 0.1$. The obtained distribution is clearly peaked at higher spin values.

There are two important aspects to addressing this issue. First and foremost, as we have stressed previously, in many of the cases in which we have been unable to provide an initial spin constraint, this has been due to the data currently available having a relatively poor S/N. This deficiency can naturally be addressed with further long observations with existing instrumentation. The other major uncertainty on some of the individual constraints obtained in this work is the cross-normalization of the XIS and PIN instruments. In order to address this issue, it will be vital to obtain observations of nearby active galaxies with the upcoming *NuStar* observatory (Harrison et al. 2010), which is due to begin operation imminently. *NuStar* will offer continuous spectral coverage over the 5–80 keV energy range, which includes a key region of overlap with the soft X-ray spectrometers currently available, and being an imaging spectrometer will allow simultaneous measurement of the background emission. Simultaneous *NuStar* and either *XMM–Newton* or *Suzaku* observations will be able to provide spin measurements robust to the current cross-calibrational uncertainties. In addition, the microcalorimeter due to fly aboard *Astro-H* (2014; Kokubun et al. 2008) will enable the profiles of the soft excesses and the iron lines to be resolved in much greater detail, enabling us to further test the robustness of the reflection interpretation and improve the spin measurements obtained. Finally, the effect of any high spin bias will ultimately need to be tested in the future with large, volume-limited samples of AGN.

5 CONCLUSIONS

We have investigated the relativistic disc reflection interpretation for a large sample of 25 'bare' AGN, sources with little or no complicating intrinsic absorption, observed with *Suzaku*. In constructing reflection-based models for this sample, we have taken the unique approach of attempting to simultaneously undertake a systematic analysis of the whole sample as well as a detailed treatment of each individual source, and find that disc reflection has the required flexibility to successfully reproduce the broad-band spectra of all of the sources considered. Where possible, we also use the reflected emission to place constraints on the black hole spin for this sample of sources. Our analysis suggests a general preference for rapidly rotating black holes, which if taken at face value is most consistent with the scenario in which SMBH growth is dominated by prolonged, ordered accretion. However, there may be strong observational biases towards AGN with high spin in the compiled sample, which limits our ability to draw strong conclusions for the overall population at this stage. Our analysis also implies that the radio-loud/radio-quiet AGN dichotomy is not related to black hole spin.

ACKNOWLEDGMENTS

This research has made use of data obtained from the *Suzaku* observatory, a collaborative mission between the space agencies of Japan (JAXA) and the USA (NASA). DJW acknowledges the financial support provided by STFC in the form of a PhD scholarship, EN is supported by NASA grants GO2-13124X and NNX11AG99G, and ACF thanks the Royal Society. RCR thanks the Michigan Society of Fellows, and is supported by NASA through the Einstein Fellowship Program, grant number PF1-120087. Special thanks go to both Jeremy Sanders and Jack Steiner for their computational assistance, which greatly aided in the publication of this research. The figures included in this work have been produced with the VEUSZ[7] plotting package, written by Jeremy Sanders. Finally, the authors would like to thank the referee for their feedback, which helped improve the depth of this work.

REFERENCES

Arnaud K. A., 1996, in Jacoby G. H., Barnes J., eds, ASP Conf. Ser. Vol. 101, Astronomical Data Analysis Software and Systems V. Astron. Soc. Pac., San Francisco, p. 17
Bardeen J. M., Press W. H., Teukolsky S. A., 1972, ApJ, 178, 347
Beloborodov A. M., 1999, ApJ, 510, L123
Berti E., Volonteri M., 2008, ApJ, 684, 822
Blandford R. D., 1990, in Blandford R. D., Netzer H., Woltjer L., Courvoisier T. J.-L., Mayor M., eds, Active Galactic Nuclei. Berlin, Springer, p. 161
Blandford R. D., Znajek R. L., 1977, MNRAS, 179, 433
Blustin A. J. et al., 2007, A&A, 466, 107
Boldt E., 1987, in Hewitt A., Burbidge G., Fang L. Z., eds, Proc. IAU Symp. 124, Observational Cosmology. IAU, p. 611
Boller T. et al., 2002, MNRAS, 329, L1

[7] http://home.gna.org/veusz/

Boller T., Tanaka Y., Fabian A., Brandt W. N., Gallo L., Anabuki N., Haba Y., Vaughan S., 2003, MNRAS, 343, L89
Brenneman L. W., Reynolds C. S., 2006, ApJ, 652, 1028
Brenneman L. W. et al., 2011, ApJ, 736, 103
Cowperthwaite P. S., Reynolds C. S., 2012, ApJ, 752, L21
Crummy J., Fabian A. C., Gallo L., Ross R. R., 2006, MNRAS, 365, 1067
Dauser T., Wilms J., Reynolds C. S., Brenneman L. W., 2010, MNRAS, 409, 1534
Dauser T. et al., 2012, MNRAS, 422, 1914
de Marco B., Ponti G., Uttley P., Cappi M., Dadina M., Fabian A. C., Miniutti G., 2011, MNRAS, 417, L98
De Marco B., Ponti G., Cappi M., Dadina M., Uttley P., Cackett E. M., Fabian A. C., Miniutti G., 2012, arXiv:1201.0196
Detmers R. G. et al., 2011, A&A, 534, A38
Dewangan G. C., Griffiths R. E., Dasgupta S., Rao A. R., 2007, ApJ, 671, 1284
Done C., Davis S. W., Jin C., Blaes O., Ward M., 2012, MNRAS, 420, 1848
Emmanoulopoulos D., Papadakis I. E., McHardy I. M., Nicastro F., Bianchi S., Arévalo P., 2011a, MNRAS, 415, 1895
Emmanoulopoulos D., McHardy I. M., Papadakis I. E., 2011b, MNRAS, 416, L94
Fabian A. C., Rees M. J., Stella L., White N. E., 1989, MNRAS, 238, 729
Fabian A. C., Iwasawa K., Reynolds C. S., Young A. J., 2000, PASP, 112, 1145
Fabian A. C., Miniutti G., Gallo L., Boller T., Tanaka Y., Vaughan S., Ross R. R., 2004, MNRAS, 353, 1071
Fabian A. C., Miniutti G., Iwasawa K., Ross R. R., 2005, MNRAS, 361, 795
Fabian A. C. et al., 2009, Nat, 459, 540
Fabian A. C. et al., 2012a, arXiv:1208.5898
Fabian A. C. et al., 2012b, MNRAS, 419, 116
Fender R. P., Belloni T. M., Gallo E., 2004, MNRAS, 355, 1105
Gallo L. C., Fabian A. C., 2011, MNRAS, 418, L59
Gallo L. C., Tanaka Y., Boller T., Fabian A. C., Vaughan S., Brandt W. N., 2004, MNRAS, 353, 1064
Gallo L. C. et al., 2012, arXiv:1210.0855
Garofalo D., Evans D. A., Sambruna R. M., 2010, MNRAS, 406, 975
George I. M., Fabian A. C., 1991, MNRAS, 249, 352
Gierliński M., Done C., 2004, MNRAS, 349, L7
Giovannini G., Cotton W. D., Feretti L., Lara L., Venturi T., 2001, ApJ, 552, 508
Gliozzi M., Papadakis I. E., Grupe D., Brinkmann W. P., Raeth C., Kedziora-Chudczer L., 2010, ApJ, 717, 1243
Gondoin P., Lumb D., Siddiqui H., Guainazzi M., Schartel N., 2001, A&A, 373, 805
Grupe D., Komossa S., Gallo L. C., Fabian A. C., Larsson J., Pradhan A. K., Xu D., Miniutti G., 2008, ApJ, 681, 982
Harrison F. A. et al., 2010, Proc. SPIE, 7732, 27
Jin C., Ward M., Done C., 2012, MNRAS, 425, 907
Kaastra J. S. et al., 2011, A&A, 534, A37
Kalberla P. M. W., Burton W. B., Hartmann D., Arnal E. M., Bajaja E., Morras R., Pöppel W. G. L., 2005, A&A, 440, 775
Kallman T., Bautista M., 2001, ApJS, 133, 221
Kallman T. R., Palmeri P., Bautista M. A., Mendoza C., Krolik J. H., 2004, ApJS, 155, 675
Kara E., Fabian A. C., Cackett E. M., Steiner J. F., Uttley P., Wilkins D. R., Zoghbi A., 2012, arXiv:1210.1465
Kokubun M. et al., 2008, Proc. SPIE, 7011, 21
Laor A., 1991, ApJ, 376, 90
Longinotti A. L. et al., 2010, A&A, 510, A92
Magdziarz P., Zdziarski A. A., 1995, MNRAS, 273, 837
Markoff S., Nowak M. A., Wilms J., 2005, ApJ, 635, 1203
Matt G., Fabian A. C., Ross R. R., 1993, MNRAS, 262, 179
Middleton M., Done C., Gierliński M., 2007, MNRAS, 381, 1426
Miller L., Turner T. J., Reeves J. N., 2008, A&A, 483, 437
Miller L., Turner T. J., Reeves J. N., 2009, MNRAS, 399, L69
Miller L., Turner T. J., Reeves J. N., Braito V., 2010, MNRAS, 408, 1928
Miniutti G., Fabian A. C., 2004, MNRAS, 349, 1435
Miniutti G., Ponti G., Greene J. E., Ho L. C., Fabian A. C., Iwasawa K., 2009, MNRAS, 394, 443
Miniutti G., Piconcelli E., Bianchi S., Vignali C., Bozzo E., 2010, MNRAS, 401, 1315
Moderski R., Sikora M., 1996, A&AS, 120, C591
Moderski R., Sikora M., Lasota J.-P., 1998, MNRAS, 301, 142
Nandra K., George I. M., Mushotzky R. F., Turner T. J., Yaqoob T., 1999, ApJ, 523, L17
Nandra K., O'Neill P. M., George I. M., Reeves J. N., 2007, MNRAS, 382, 194
Nardini E., Fabian A. C., Reis R. C., Walton D. J., 2011, MNRAS, 410, 1251
Nardini E., Fabian A. C., Walton D. J., 2012, MNRAS, 423, 3299
Patrick A. R., Reeves J. N., Lobban A. P., Porquet D., Markowitz A. G., 2011a, MNRAS, 416, 2725
Patrick A. R., Reeves J. N., Porquet D., Markowitz A. G., Lobban A. P., Terashima Y., 2011b, MNRAS, 411, 2353
Petrucci P. O. et al., 2007, A&A, 470, 889
Ponti G. et al., 2010, MNRAS, 406, 2591
Reeves J. N. et al., 2009, ApJ, 701, 493
Reis R. C. et al., 2012, ApJ, 745, 93
Reynolds C. S., Brenneman L. W., Lohfink A. M., Trippe M. L., Miller J. M., Reis R. C., Nowak M. A., Fabian A. C., 2012, in Petre R., Mitsuda K., Angelini L., eds, AIP Conf. Ser. Vol. 1427, Suzaku 2011: Exploring the X-ray Universe. Am. Inst. Phys., New York, p. 157
Ross R. R., Fabian A. C., 2005, MNRAS, 358, 211
Ross R. R., Fabian A. C., Brandt W. N., 1996, MNRAS, 278, 1082
Sambruna R. M. et al., 2009, ApJ, 700, 1473
Sambruna R. M., Tombesi F., Reeves J. N., Braito V., Ballo L., Gliozzi M., Reynolds C. S., 2011, ApJ, 734, 105
Schmoll S. et al., 2009, ApJ, 703, 2171
Schurch N. J., Done C., 2007, MNRAS, 381, 1413
Schurch N. J., Done C., Proga D., 2009, ApJ, 694, 1
Steiner J. F., McClintock J. E., 2012, ApJ, 745, 136
Tanaka Y. et al., 1995, Nat, 375, 659
Tombesi F., Cappi M., Reeves J. N., Palumbo G. G. C., Yaqoob T., Braito V., Dadina M., 2010, A&A, 521, A57
Torresi E., Grandi P., Longinotti A. L., Guainazzi M., Palumbo G. G. C., Tombesi F., Nucita A., 2010, MNRAS, 401, L10
Vaughan S., Boller T., Fabian A. C., Ballantyne D. R., Brandt W. N., Trümper J., 2002, MNRAS, 337, 247
Vaughan S., Fabian A. C., Ballantyne D. R., De Rosa A., Piro L., Matt G., 2004, MNRAS, 351, 193
Volonteri M., Madau P., Quataert E., Rees M. J., 2005, ApJ, 620, 69
Walton D. J., Reis R. C., Fabian A. C., 2010, MNRAS, 408, 601
Walton D. J., Reis R. C., Cackett E. M., Fabian A. C., Miller J. M., 2012, MNRAS, 422, 2510
Wang J., Fabbiano G., Elvis M., Risaliti G., Mazzarella J. M., Howell J. H., Lord S., 2009, ApJ, 694, 718
Wilkins D. R., Fabian A. C., 2011, MNRAS, 414, 1269
Wilms J., Allen A., McCray R., 2000, ApJ, 542, 914
Wilson A. S., Colbert E. J. M., 1995, ApJ, 438, 62
Zoghbi A., Fabian A. C., 2011, MNRAS, 418, 2642
Zoghbi A., Fabian A. C., Uttley P., Miniutti G., Gallo L. C., Reynolds C. S., Miller J. M., Ponti G., 2010, MNRAS, 401, 2419
Zoghbi A., Fabian A. C., Reynolds C. S., Cackett E. M., 2012, MNRAS, 422, 129

APPENDIX A: MULTIPARAMETER REFLECTION MODELS

One of the major aspects ofthis work is attempting to constrain the black hole spin from the full contribution of the reflected emission from the accretion disc observed in AGN, i.e. from the combination of the soft excess, any broadened iron K emission and the high-energy reflected continuum. In order to do so, we make use of a physically self-consistent reflection model, REFLIONX (Ross

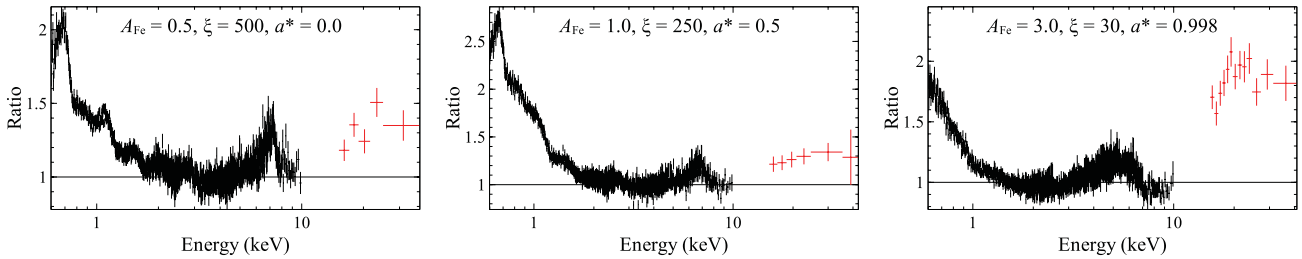

Figure A1. Data/model ratio plots for a selection of the simulated *Suzaku* XIS (front illuminated; black) and PIN (red) spectra to a simple power-law continuum model. The plots for the two higher spin values shown display reasonable qualitative similarities with many of the real data sets shown in Fig. 1. The simulated data shown have been rebinned for plotting purposes only.

Table A1. The various input parameter combinations simulated, and the values obtained modelling these simulated spectra with our PLC+RDC continuum; all the spectra are simulated with $\Gamma = 2.0$, $q = 6$ and $i = 45^\circ$. The input parameters are generally successfully reproduced.

Input parameters			Values obtained					
A_{Fe} (solar)	ξ (erg cm s^{-1})	a^*	Γ	i (°)	q	A_{Fe} (solar)	ξ (erg cm s^{-1})	a^*
0.5	30	0	2.00 ± 0.01	45^{+2}_{-1}	>3.4	$0.50^{+0.05}_{-0.04}$	33^{+4}_{-3}	$0.02^{+0.18}_{-0.25}$
0.5	30	0.5	2.00 ± 0.01	44^{+3}_{-2}	$5.3^{+1.4}_{-0.8}$	0.5 ± 0.1	32^{+5}_{-3}	$0.46^{+0.11}_{-0.10}$
0.5	30	0.998	$2.00^{+0.02}_{-0.04}$	41^{+9}_{-4}	$5.5^{+1.2}_{-0.6}$	$0.5^{+0.3}_{-0.1}$	34^{+19}_{-9}	>0.97
0.5	250	0	2.01 ± 0.01	45^{+2}_{-1}	$4.2^{+2.4}_{-1.0}$	0.48 ± 0.02	246 ± 6	$0.24^{+0.16}_{-0.28}$
0.5	250	0.5	2.01 ± 0.01	42^{+7}_{-3}	>4.3	0.54 ± 0.04	243 ± 6	$0.28^{+0.31}_{-0.22}$
0.5	250	0.998	$2.01^{+0.02}_{-0.01}$	45^{+3}_{-9}	$6.3^{+1.1}_{-0.9}$	$0.47^{+0.05}_{-0.03}$	250 ± 20	>0.98
0.5	500	0	2.00 ± 0.01	46^{+2}_{-1}	>5.7	0.52 ± 0.02	500^{+10}_{-50}	$0.05^{+0.25}_{-0.14}$
0.5	500	0.5	2.01 ± 0.01	$46^{+4}_{-3.}$	>5.8	0.51 ± 0.02	450^{+50}_{-40}	$0.52^{+0.23}_{-0.18}$
0.5	500	0.998	2.01 ± 0.01	48 ± 7	$6.8^{+1.5}_{-1.0}$	$0.48^{+0.05}_{-0.04}$	460^{+60}_{-80}	>0.98
1	30	0	2.00 ± 0.01	46^{+1}_{-2}	>4.8	$1.00^{+0.09}_{-0.045}$	30 ± 2	$0.04^{+0.15}_{-0.24}$
1	30	0.5	2.00 ± 0.01	44 ± 2	$5.8^{+1.0}_{-0.8}$	1.0 ± 0.1	30^{+4}_{-3}	0.46 ± 0.08
1	30	0.998	2.01 ± 0.03	41^{+6}_{-4}	$5.4^{+1.0}_{-0.5}$	$1.1^{+0.2}_{-0.1}$	26^{+8}_{-4}	>0.98
1	250	0	$2.006^{+0.003}_{-0.005}$	46 ± 1	>6.5	0.98 ± 0.03	252^{+2}_{-5}	$-0.11^{+0.18}_{-0.12}$
1	250	0.5	2.01 ± 0.01	44^{+6}_{-3}	>4.7	1.1 ± 0.1	251 ± 6	$0.42^{+0.26}_{-0.19}$
1	250	0.998	2.02 ± 0.01	39^{+9}_{-8}	$5.7^{+1.3}_{-0.9}$	$1.0^{+0.2}_{-0.1}$	240 ± 10	>0.97
1	500	0	2.00 ± 0.01	46^{+2}_{-1}	>4.6	1.1 ± 0.1	510 ± 10	$0.11^{+0.22}_{-0.30}$
1	500	0.5	2.01 ± 0.01	43^{+7}_{-2}	$5.4^{+4.1}_{-1.2}$	1.0 ± 0.1	490^{+20}_{-40}	$0.41^{+0.27}_{-0.16}$
1	500	0.998	2.00 ± 0.01	45^{+4}_{-5}	$6.0^{+0.7}_{-0.6}$	$1.0^{+0.2}_{-0.1}$	510 ± 10	>0.98
3	30	0	2.00 ± 0.01	44 ± 1	$6.4^{+2.0}_{-1.3}$	2.9 ± 0.2	32^{+3}_{-2}	$-0.13^{+0.13}_{-0.18}$
3	30	0.5	2.00 ± 0.01	47 ± 2	7.0 ± 1.0	3.3 ± 0.2	31^{+3}_{-2}	$0.57^{+0.07}_{-0.10}$
3	30	0.998	1.99 ± 0.03	42 ± 3	5.5 ± 0.4	3.6 ± 0.4	31^{+17}_{-5}	>0.98
3	250	0	2.01 ± 0.01	45^{+3}_{-1}	>4.1	3.2 ± 0.2	250 ± 5	$0.01^{+0.41}_{-0.31}$
3	250	0.5	2.00 ± 0.01	47^{+3}_{-2}	>6.1	2.9 ± 0.2	244^{+5}_{-4}	$0.53^{+0.14}_{-0.13}$
3	250	0.998	2.00 ± 0.01	48 ± 6	$6.7^{+1.3}_{-0.9}$	$3.3^{+0.2}_{-0.4}$	280 ± 20	>0.97
3	500	0	2.01 ± 0.01	45 ± 1	$6.1^{+3.5}_{-1.9}$	3.0 ± 0.1	500^{+10}_{-20}	$-0.06^{+0.25}_{-0.24}$
3	500	0.5	2.01 ± 0.01	47 ± 2	$7.7^{+1.6}_{-1.3}$	3.0 ± 0.1	500^{+10}_{-30}	0.53 ± 0.10
3	500	0.998	2.01 ± 0.01	49^{+3}_{-4}	6.8 ± 0.7	3.5 ± 0.5	510^{+10}_{-90}	>0.99

& Fabian 2005), combined with the latest relativistic convolution kernal, RELCONV (Dauser et al. 2010). This combination results in a complex, multiparameter model for the reflected emission observed, including the ionization of the surface of the disc, its iron abundance, the radial emissivity profile, the disc inclination and of course the black hole spin. The combination of the ionization parameter and the iron abundance in particular can have a strong effect on the broad-band spectral shape. In order to simultaneously constrain all of these parameters, some balance between the strength of the reflection features and the quality of data available is naturally required. In this appendix, we present a series of simulations demonstrating that reasonable quality *Suzaku* data can provide reliable constraints for all of these parameters.

Using the FAKEIT command in XSPEC, we simulate *Suzaku* data based on our underlying PLC+RDC continuum model (modified by neutral absorption), using standard response and background files for the (front illuminated) XIS and PIN detectors. These spectra are rebinned to the same S/N requirements as the real data presented

in the main body of the paper, i.e. a minimum S/N per energy bin of 5 for the combined FI XIS spectra, and 3 for the PIN spectra. The 2–10 keV flux for the PLC component in these models is set to 2×10^{-11} erg cm^{-2} s^{-1}, and for simplicity both the PLC and RDC components are required to contribute the same flux over the much broader 0.1–1000.0 keV energy range (i.e. the energy range over which the version of the REFLIONX model utilized here is calculated). The exposure time for the simulations is set to 125 ks, such that we are simulating a fairly good *Suzaku* observation of a fairly bright AGN, relative to the sample compiled. We repeat this process for a variety of input parameter combinations, varying the ionization of the disc, the iron abundance and the black hole spin. The other key parameters adopted are $N_{\rm H} = 3 \times 10^{20}$ atom cm^{-2}, $\Gamma = 2$, $q = 6$, $i = 45^{\circ}$, relatively typical of the results obtained in the main body of the paper. For illustration, Fig. A1 shows some examples of the ratio plots obtained with the simulated spectra when modelled with a simple absorbed power-law model, applied as described in Section 2.2. The plots obtained for the two higher spin values, although obviously showing idealized scenarios in which just the PLC and disc reflection components are present, are reasonably similar to many of those obtained with the real data (see Fig. 1). Each of the simulated spectra are then modelled with our PLC+RDC continuum model, and the parameters obtained are presented in Table A1.

In general, the input parameters are successfully reproduced, particularly the parameters that significantly help determine the broad-band spectral shape, i.e. the iron abundance, disc ionization and photon index. The relativistic blurring parameters are also generally well reproduced, although there is one interesting trend worth briefly discussing. It is clear from Table A1 that it is easier to constrain the spin when the spin is high. This can be understood in terms of the evolution of the theoretical relation between the radius of the ISCO with black hole spin (see Bardeen et al. 1972). At higher spins, a given deviation in spin results in larger deviations in the radius of the ISCO. As the model utilized here ultimately infers the spin by determining the inner radius of the disc from the observed spectrum, and assumes this is coincident with the ISCO, it is therefore naturally easier to statistically constrain higher spins via this method. Nevertheless, these simulations demonstrate that *Suzaku* data with reasonably good S/N (as well as reasonably strong reflection features) should be sufficient to determine even moderate spins, as well as the other key parameters of interest in this work, from the observed broad-band X-ray spectrum.

This paper has been typeset from a TEX/LATEX file prepared by the author.